

---

# COMPUTATIONAL MAPPING OF THE HUMAN-SARS-CoV-2 PROTEIN-RNA INTERACTOME

---

A bioRxiv PREPRINT

Marc Horlacher<sup>1</sup>, Svitlana Oleshko<sup>1</sup>, Yue Hu<sup>1</sup>, Mahsa Ghanbari<sup>2</sup>, Giulia Cantini<sup>1</sup>, Patrick Schinke<sup>1</sup>,  
Ernesto Elorduy Vergara<sup>1</sup>, Florian Bittner<sup>3</sup>, Nikola S. Mueller<sup>3</sup>, Uwe Ohler<sup>2</sup>,  
Lambert Moyon<sup>1,\*</sup>, Annalisa Marsico<sup>1,\*</sup>

**1 Computational Health Center, Helmholtz Center Munich, Germany**

**2 Berlin Institute for Medical Systems Biology, Max Delbrück Center for Molecular Medicine, Berlin, Germany**

**3 Knowing01 GmbH, Munich, Germany**

\* [lambert.moyon@helmholtz-muenchen.de](mailto:lambert.moyon@helmholtz-muenchen.de) and [annalisa.marsico@helmholtz-muenchen.de](mailto:annalisa.marsico@helmholtz-muenchen.de)

May 4, 2022

## ABSTRACT

1 Strong evidence suggests that human RNA-binding proteins (RBPs) are critical factors for  
2 viral infection, yet there is no feasible experimental approach to map exact binding sites of RBPs  
3 across the SARS-CoV-2 genome systematically at a large scale. We investigated the role of RBPs  
4 in the context of SARS-CoV-2 by constructing the first in silico map of human RBP / viral RNA  
5 interactions at nucleotide-resolution using two deep learning methods (pysster and DeepRiPe) trained  
6 on data from CLIP-seq experiments. We evaluated conservation of RBP binding between 6 other  
7 human pathogenic coronaviruses and identified sites of conserved and differential binding in the  
8 UTRs of SARS-CoV-1, SARS-CoV-2 and MERS. We scored the impact of variants from 11 viral  
9 strains on protein-RNA interaction, identifying a set of gain-and loss of binding events. Lastly, we  
10 linked RBPs to functional data and OMICs from other studies, and identified MBNL1, FTO and  
11 FXR2 as potential clinical biomarkers. Our results contribute towards a deeper understanding of  
12 how viruses hijack host cellular pathways and are available through a comprehensive online resource  
13 (<https://sc2rbpmap.helmholtz-muenchen.de>).

14 **Keywords** SARS-CoV-2 · RBP binding · deep learning

## COMPUTATIONAL MAPPING OF THE HUMAN-SARS-CoV-2 PROTEIN-RNA INTERACTOME

### 15 **1 Introduction**

16 SARS-CoV-2, causative agent of the recent COVID-19 pandemic, has and still is affecting the lives of billions of people  
17 worldwide. Despite the large-scale vaccination effort, the number of infections and deaths remains high, primarily  
18 among the non-vaccinated and otherwise vulnerable individuals. Difficulty to control SARS-CoV-2 infections is  
19 partly due to the continuous emergence of novel viral variants, against which the full efficacy of current vaccines  
20 is still debated, as well as the lack of effective medication. This calls for a better understanding of the biology of  
21 SARS-CoV-2 to design alternative therapeutic strategies. SARS-CoV-2 is a betacoronavirus with a positive-sense,  
22 single-stranded RNA of ~30kb (90). Upon infection, the released RNA molecule depends on the host cell's protein  
23 synthesis machinery to express a set of viral proteins crucial for replication (73). The genomic RNA is translated  
24 to produce non-structural proteins (nsps) from two open reading frames (ORFs), ORF1a and ORF1b, and it also  
25 contains untranslated regions (UTRs) at the 5' and 3' ends of the genomic RNA (90). A recent study revealed the  
26 complexity of the SARS-CoV-2 transcriptome, due to numerous discontinuous transcription events (39). Negative sense  
27 RNA intermediates are generated to serve as the template for the synthesis of positive-sense genomic RNA (gRNA)  
28 and subgenomic RNAs (sgRNA) which encode conserved structural proteins (spike protein [S], envelop protein [E],  
29 membrane protein [M] and nucleocapsid protein [N]), and several accessory proteins (3a, 6, 7a, 7b, 8 and 10) (39).  
30 During its life cycle, SARS-CoV-2 extensively interacts with host factors in order to facilitate cell entry, transcription  
31 of viral RNA and translation of subgenomic mRNAs, virion maturation and evasion of the host's immune response  
32 (90; 11; 20). Mechanisms of virus-host interaction are multifaceted and include protein-protein interactions (PPIs),  
33 binding of viral proteins to the host transcriptome (96), RNA-RNA interactions and binding of host proteins to viral  
34 RNAs. Studies on SARS-CoV-2 infected cells to date have predominantly focused on the entry of SARS-CoV-2 into  
35 human epithelial cells, which involves the interaction of the viral spike protein S with the human ACE2 receptor  
36 (39). Other studies characterized changes in the host cell transcriptome and proteome upon infection and identified  
37 host factors essential for viral replication via CRISPR screenings (78; 25; 92). Lastly, mapping of protein-protein  
38 interactions (PPIs) between viral and host proteins has revealed cellular pathways important for SARS-CoV-2 infection.  
39 For instance, a recent study identified close to 300 host-virus interactions in the context of SARS-CoV-2 (25). However,  
40 these studies have been of limited impact with respect to revealing how the viral RNA is regulated during infection.

41 RNA viruses hijack key cellular host pathways by interfering with the activity of master regulatory proteins, including  
42 RNA binding proteins (RBPs) (29). RBPs are a family of proteins that bind to RNA molecules and control several  
43 aspects of cellular RNA metabolism, including splicing, stability, export and translation initiation. In most cases,  
44 RNA targets of an RBP share at least one common local sequence or structural feature – a so-called motif - which  
45 facilitates the recognition of the RNA by the protein. Host cell RBPs have previously been reported to interact with  
46 viral RNA elements and influence several steps of the viral life cycle, such as recruitment of viral RNA to the membrane  
47 and synthesis of subgenomic viral RNAs (47; 48; 59; 21). Indeed, in a recent proteome-wide study, 342 RBPs were  
48 identified to be annotated with gene ontology (GO) terms related to viruses, infection or immunity with a further 130  
49 RBPs being linked to viruses in literature (21). Examples include the Dengue virus Manokaran et al. (56), the Murine  
50 Norovirus (MNV) (88) and Sindbis virus (SINV), where it has been shown that RBPs stimulated by the infection  
51 redistribute to viral replication factories and modulate the success of infection (21). The ability of viral RNAs to  
52 recruit essential host RBPs could explain permissiveness of certain cell types as well as its range of hosts (48), which  
53 is especially relevant for zoonotic viruses such as SARS-CoV-2. In the context of SARS-CoV infection, DEAD-box  
54 helicase 1 (DDX1) RBP has been shown to facilitate template read-through and thus replication of genomic viral  
55 RNA, while heterogeneous nuclear ribonucleoprotein A1 (hnRNPA1) might regulate viral RNA synthesis (20; 54; 94).  
56 Multiple recent studies show that SARS-CoV-2 RNAs extensively interact with both pro- and anti-viral host RBPs  
57 during its life cycle (18; 69; 46; 43). Using comprehensive identification of RNA-binding proteins by mass spectrometry  
58 (ChIRP-MS), Flynn et al. (18) identified a total of 229 vRNA-bound host factors in human Huh7.5 cells with prominent  
59 roles in protecting the host from virus-induced cell death. Schmidt et al. (69) identified 104 vRNA-bound human  
60 proteins in the same cell line via RNA antisense purification and quantitative mass spectrometry (RAP-MS), with  
61 GO-terms strongly enriched in translation initiation, nonsense-mediated decay and viral transcription. The authors  
62 further confirmed the specific location of vRNA binding sites for cellular nucleic acid-binding protein (CNBP) and  
63 La-related protein 1 (LARP1) via enhanced cross-linking immunoprecipitation followed by sequencing (eCLIP-seq),  
64 which were both associated to restriction of SARS-CoV-2 replication (69). Lee et al. (46) identified 109 vRNA-bound  
65 proteins via a modified version of the RAP-MS protocol and linked those RBPs to RNA stability control, mRNA  
66 function, and viral process. Further, the authors showed 107 of those host factors are found to interact with vRNA of  
67 the seasonal betacoronavirus HCoV-OC43, suggesting that the vRNA interactome is highly conserved. Finally, Labeau  
68 et al. (43) used ChIRP-MS to identify 142 host proteins that bind to the SARS-CoV-2 RNA and showed, in contrast  
69 to Flynn et al. (18), that siRNA knockdown of most RBPs cellular expression leads to a significant reduction in viral  
70 particles, suggesting that the majority of RBPs represent pro-viral factors. Taken together, there is strong evidence that  
71 SARS-CoV-2, like other RNA viruses, heavily relies on the presence of a large number of essential RNA-binding host

## COMPUTATIONAL MAPPING OF THE HUMAN-SARS-CoV-2 PROTEIN-RNA INTERACTOME

72 factors. However, the sets of SARS-CoV-2 relevant RBPs from different studies have limited overlap and the outcome  
73 depends on the specific cell line utilized in the experiment. Further, most studies lack information of exact binding  
74 sites of human RBPs on viral RNA. A comprehensive large scale analysis of the propensities of different host RBPs to  
75 bind to RNA elements across the SARS-CoV-2 genome is currently missing.

76 Cross-linking and immunoprecipitation (IP) followed by sequencing (CLIP-seq) assays (26), including PAR-CLIP  
77 and eCLIP protocols, are the most widely used methods to measure RBP-RNA interactions *in vivo* at high nucleotide  
78 resolution and are able to provide sets of functional elements that are directly bound by an RBP of interest (85). While  
79 CLIP-seq experiments allow for precise identification of host factor interaction with viral RNAs, the high cost of  
80 profiling interactions across a large number of RBPs becomes prohibitive at larger scales, as dedicated pull-down  
81 and sequencing has to be performed for each RBP individually. Therefore, such datasets have been generated only  
82 for a small number of proteins on SARS-CoV-2 (69). Further, in order to keep up with the continuous emergence of  
83 novel SARS-CoV-2 variants, CLIP-seq experiments would need to be repeated for the genome of each viral strain in  
84 order to account for (or to identify) gain-or loss-of-binding variants. Recent advances in machine-and deep-learning  
85 have enabled a cheaper but powerful alternative by computationally modeling the binding preference of RBPs using  
86 information from existing CLIP-seq datasets, such as those generated as part of the ENCODE project (86).

87 In this study, we train and optimize two recent Convolutional Neural Network (CNN) based methods, Pysster (5) and  
88 DeepRiPe (23), on hundreds of human eCLIP and PAR-CLIP datasets and use trained models to predict RBP binding  
89 on viral sequences. By that we provide, to our knowledge, the first comprehensive single-nucleotide resolution *in*  
90 *silico* map of viral RNA - host RBP interaction for SARS-CoV-2 as well as 6 other human coronaviruses and identify  
91 sequence variants which significantly alter RBP-RNA interaction across 11 different SARS-CoV-2 variants-of-concern.  
92 We recapitulate human RBPs which are predicted or experimentally determined to binding to SARS-CoV-2 by previous  
93 studies and identify novel host RBP candidates with no previously reported binding to SARS-CoV-2. We integrate  
94 knowledge of these proteins across other pathogens and highlight RBPs with clinical relevance, by annotating those that  
95 were found among SARS-CoV-2-associated genes from Genome Wide Association Studies (GWAS) (64), CRISPR  
96 studies (24; 30; 70; 91), physical binding experiments (18; 69; 89), or patient OMICS data from blood serum and  
97 plasma (10; 12; 13; 22; 57; 63; 71; 95). Finally, we perform extensive *in silico* single-nucleotide perturbations across  
98 the SARS-CoV-2 genome to identify variants that would lead to gain and/or disruption of RBP binding sites and thus  
99 may alter viral fitness.

## 100 2 Results

101 The overall workflow of our approach is summarized in Figure 1, from model training, to the *in silico* mapping of the  
102 SARS-CoV-2 RBP-RNA interactome and downstream analysis. We first obtained binding site information of publicly  
103 available eCLIP experiments of 150 RBPs from the ENCODE (86) database and pre-processed them to obtain a set  
104 of high-quality sites of protein-RNA interaction. For each RBP, a convolutional neural network (CNN) classifier to  
105 predict the likelihood of RBP-binding to an arbitrary input RNA sequence was trained using the *pysster* (5) framework,  
106 resulting in 150 *pysster* models (Figure 1a). For RBPs not contained in the ENCODE dataset, we included DeepRiPe  
107 (23) models pre-trained on 59 PAR-CLIP datasets. Next, we performed extensive model performance evaluation on  
108 custom trained *pysster* models and removed poorly performing models from downstream analysis. Using high-quality  
109 models, we predicted the likelihood of each RBP binding to individual nucleotides in the SARS-CoV-2 genome using  
110 a sliding-window scanning approach (Figure 1b, Methods 3.6). Single-nucleotide binding predictions were further  
111 annotated with empirical p-values to correct for false positive hits; and consecutive high-scoring and significant position  
112 were aggregated into larger binding-site regions. We thus constructed a comprehensive *in silico* binding map of human  
113 RBPs on the SARS-CoV-2 genome and clustered RBP binding sites across different viral genomic regions to unravel  
114 potential regulatory patterns (Figure 1b). Exploiting the capability of CNNs to learn complex sequence patterns, we  
115 additionally validated our approach by identifying known binding motifs at predicted RBP binding sites. Finally, we  
116 utilize our models to score the impact of sequence variant identified in 11 viral strains and identified conserved and  
117 novel binding sites across 6 other coronaviruses, including SARS-CoV-1 and MERS (Figure 1c).

### 118 2.1 Accurate model predictions in human and viral sequences

119 The trained *pysster* models showed a robust area-under-precision-recall-curve (auPRC) performance (Methods 3.7.1),  
120 with a median auPRC of 0.6 across all 150 trained models (Figure 2a). As models were used for scanning of the  
121 full-length viral genome (rather than classification of standalone examples), we further evaluate the model performance  
122 by computing the correlation of the predicted positive-class probabilities with observed ENCODE peaks on a hold-out  
123 set of human transcripts (Methods 3.7.2). Nearly all models showed a significant positive correlation, with a mean  
124 median Spearman correlation coefficient (SCC) across transcripts of 0.149 and a maximum median SCC of 0.38 (Figure  
125 2b), indicating that the trained models are well-suited for the task of scanning across the viral genome. Exemplary  
126 prediction tracks for two held-out human transcripts using *pysster* models of QKI and TARDBP are shown in Figure 2c.  
127 In general, we observe that models which perform well with respect to the auPRC score tend to perform well in the  
128 context of RNA sequence scanning (Figure 2d). To ensure that downstream analyses are based on a high-quality set  
129 of binding site predictions, models with a median SCC of less than 0.1 or an auPRC of less than 0.6 were discarded  
130 (Methods 3.7.2). A total of 63 high-quality *pysster* models were thus kept for predicting on the SARS-CoV-2 genome.  
131 For DeepRiPe, we relied on the results from (23) and retained only those models where informative sequence motifs  
132 were learned during training, leaving a total of 33 RBP models for predicting on the SARS-CoV-2 genome. Of those,  
133 we selected only models for RBPs not contained in the ENCODE database, leading to the addition of 24 high-quality  
134 DeepRiPe models. To confirm that *pysster* models trained on CLIP-seq data from human cell lines are suitable for  
135 cross-species binding-site inference in SARS-CoV-2, we validated our approach for RBPs with available CLIP-seq  
136 experiments from SARS-CoV-2 infected human cell lines. To this end, we obtained eCLIP datasets for CNBP and  
137 LARP1 on both human and SARS-CoV-2 transcripts from Schmidt et al. (69) and processed binding sites as described  
138 in Section 3.1. After generating training samples on CNBP and LARP1 binding sites within human transcripts (Methods  
139 3.2), we trained *pysster* models for both RBPs. We then performed prediction along the SARS-CoV-2 RNA sequence  
140 and compared the resulting prediction scores with observed binding sites as well as the raw eCLIP signal (Figure 2e,  
141 2f). Predictions from *pysster* models trained on human binding sites showed a strong correlation with the raw eCLIP  
142 signal (SCC = 0.332, p-value < 1e-16 for CNBP and SCC = 0.133, p-value = 7.96e-12 for LARP1), and accumulation  
143 of high-scoring positions at the location of called binding sites from the eCLIP experiment (Figure 2f). Further, we  
144 observed significantly higher prediction scores for in-binding-site nucleotides versus outside-binding-site nucleotides  
145 for both RBPs (Figure 2f; t-test, p-value < 1e-16 for CNBP; p-value = 2.44e-6 for LARP1). Taken together, these results  
146 strongly support the validity of our approach for cross-species *in silico* prediction of RBP binding sites.

### 147 2.2 A comprehensive *in silico* binding map of human RBPs on SARS-CoV-2

148 We performed *in silico* binding site calling by identifying consecutive significant and high-scoring positions within the  
149 SARS-CoV-2 genome with both *pysster* and DeepRiPe high-confidence models (Methods 3.9). In the following, we  
150 first demonstrate that our model predictions correspond to *bona fide* RBP binding sites on the SARS-CoV-2 genome by  
151 performing motif analysis and subsequently build a computational map of SARS-CoV-2-human RBP interactions. We  
152 then evaluate the enrichment of different RBPs for different viral genomic regions, as well as their putative regulatory  
153 function in the context of SARS-CoV-2 infection.

## COMPUTATIONAL MAPPING OF THE HUMAN-SARS-CoV-2 PROTEIN-RNA INTERACTOME

### 154 **Predicted RBP binding sites coincide with known binding motifs**

155 Figure 3a and 3b each show single-nucleotide resolution prediction scores of the well-known human RBPs RBFOX2  
156 and TARDBP, obtained from pysster models, and MBNL1 and QKI, obtained from DeepRiPe models. Identified  
157 binding sites (Methods 3.9) are shown below the prediction score tracks. To identify driving features of RBP binding  
158 and to ensure that high-scoring positions represent genuine binding sites rather than model artifacts we performed  
159 feature importance analysis (Methods 3.10) in order to assess whether the sequence features underlying the predictions  
160 at those sites correspond to the binding site preferences of those proteins reported in literature. Specifically, we centered  
161 input windows around predicted binding sites of RBFOX2, TARDBP, MBNL1 and QKI on SARS-CoV-2 to identify  
162 individual nucleotides that were most predictive for classifying the input sequence as 'bound' (Figure 3a and 3b; bottom  
163 track). We observed that feature importance maps around predicted binding sites corresponded to known binding motifs.  
164 For instance, we observe the well-known consensus sequence (T)GCATG recognized by the splicing factor RBFOX2  
165 (36) in the corresponding feature importance maps (Figure 3a, left), as well as the TG-repeat motif, corresponding  
166 to the sequence preference of TARDBP (28), coinciding with its predicted binding sites (Figure 3a, right). Similarly,  
167 DeepRiPe attribution maps with respect to binding sites of QKI show the canonical binding motif TACTAA(C) (82)  
168 (Figure 3b, left). Lastly, the attribution maps computed at each binding site of the splicing factor MBNL1 all harbour  
169 occurrences of the characteristic YGCY motif (45) (Figure 3b, right).

### 170 **Binding site predictions are robust across different datasets and prediction tools**

171 To evaluate the robustness of viral binding site predictions across pysster and DeepRiPe, we compared predictions for a  
172 small set of RBPs where both eCLIP data (used to train a pysster models) and PAR-CLIP data (used for the training of  
173 DeepRiPe models) were available. Among a total of 20 overlapping RBPs, 12 were contained in the sets of high-quality  
174 models for pysster and DeepRiPe selected in 2.1, namely TARDBP, CSTF2, IGF2BP1, PUM2, CSTF2T, QKI, IGF2BP2,  
175 IGF2BP3, CPSF6 FXR1, FXR2 and EWSR1. For each of the 12 RBPs, we then computed the Spearman correlation  
176 between the pysster and DeepRiPe prediction scores across single-nucleotide positions on the viral genome. We  
177 observed a signal correlation higher than 0.1 for 8 out of the 12 RBPs, with a Spearman correlation coefficient ranging  
178 from a maximum of 0.64 (TARDBP) to a minimum of 0.15 (CPSF6) (Supplementary Table 1). In general, we observed  
179 a higher overlap between pysster and DeepRiPe binding site predictions for RBPs harbouring well-defined RNA  
180 sequence motifs, such as QKI, TARDBP, PUM2, CSTF2, and to a less extent, FXR1/2 and IGF2BP1/2/3. In addition,  
181 feature attributions maps at overlapping binding sites of pysster and DeepRiPe with respect to QKI and TARDBP  
182 (Supplementary Figure 1), highlight the presence of the known binding motifs for these two RBPs.

### 183 **Binding preferences and clusters of human RBP predicted sites on the SARS-CoV-2 genome**

184 Given the strong evidence that our predictions reflect true likelihoods of viral sequence regions being bound by human  
185 RBPs, we set out to build a full *in silico* SARS-CoV-2 / human RBP binding map, using the set of 88 high confidence  
186 models from both pysster and DeepRiPe (Section 2.1). Note that we included the CNBP model from Section 2.1, as it  
187 satisfied our performance constrains. Further, for the 12 shared RBPs between pysster and DeepRiPe, only pysster  
188 predictions were considered for downstream analysis, given the high agreement between both models. Figure 3c (right)  
189 depicts the binding profiles of 84 (out of 88) human RBPs which harbor at least one binding site on the SARS-CoV-2  
190 sequence. We clustered RBPs into eight classes based on their relative binding site coverage across different genomic  
191 regions of the SARS-CoV-2 genome (Figure 3c, left). We observe that some clusters of proteins exhibit sparse binding  
192 signal across the SARS-CoV-2 genome (such as clusters 2 and 3), while other clusters contain RBPs which are predicted  
193 to bind extensively across the whole SARS-CoV-2 genome (cluster 4). Interestingly, some clusters harbour RBPs  
194 shown to preferentially bind specific genomic elements (cluster 1 and cluster 5-8, Figure 3c, left). We observe overall  
195 extensive RBP binding coverage mostly at 5' UTRs and genomic regions coding for E, M and N structural proteins, and  
196 less coverage at the spike S gene, as well as the viral 3' UTR. To some extent, clustering of predicted binding sites  
197 groups together RBPs with similar functions in RNA processing and viral regulation, as well similar RNA recognition  
198 mechanisms. Cluster 4 corresponds to a group of well-known regulators of RNA processing, which extensively bind  
199 the viral 5' UTR, as well as the ORF1ab and subgenomic RNAs. This includes proteins from the FXR family (FXR1,  
200 FXR2 and FMR1), which recognize RNA using the K Homology (KH) domain, and control RNA stability, translation  
201 and RNA localization (85). Other RNA translational regulators in the same cluster include the DDX3X helicase, which  
202 was recently identified as host target against SARS-CoV-2 infection (9), and the 40S ribosomal protein S3 (RPS3),  
203 which also binding RNAs through the KH domain. Other proteins in this cluster with well-known roles in regulation  
204 of viral infections are SND1, the splicing regulators (SR) SRSF1 and SRSF2, shown to be implicated in increasing  
205 translation efficiency in the context of HIV infection (55), the RNA demethylase factor FTO, known to regulate viral  
206 infections and HIV-1 protein expression (83), in addition to the aforementioned G3BP1 and DDX3X involved in innate  
207 immunity (8). Cluster 1 predominantly harbors RBPs with binding preference for the viral 3' UTR, including regulators  
208 of RNA stability and proteins involved in 3' end formation and/or regulation of translation. Among those RBPs, the

## COMPUTATIONAL MAPPING OF THE HUMAN-SARS-CoV-2 PROTEIN-RNA INTERACTOME

209 poly (I:C) binding protein KHDRBS1 has been identified to have pro-viral activity in SFV infection (65), while the  
210 multifunctional RBP PCBP1, along with hnRNPs has been shown to be implicated in translational control of many  
211 viruses, including poliovirus, human papilloma virus and Hepatitis A virus. Cluster 6 is comprised of RBPs which  
212 preferentially bind to the 5' UTR of SARS-CoV-2. Interestingly, these proteins (AQR, GPKOW, SF3A3, SF3B4 and  
213 A2AF2) are known to be functionally involved in splicing and harbour a RNA recognition motif (RRM) (85). We  
214 find that cluster 6 also harbors NONO, a member of the paraspeckle complex, which has previously been associated  
215 with antiviral immune response and which is part of the RBP interactome in SINV infected cells (21), as well as  
216 TARDBP, a protein that localizes to P-bodies and stress granules and was shown to bind to the 5' UTR of SARS-CoV-2  
217 in a recent study (60). Cluster 5 includes a large class of RBPs with diverse functions, including splicing (SRSF9),  
218 post-transcriptional repression (PUM2 and CAPRIN1), snoRNA binding (NOP58 and NIP7) and miRNA-mediated  
219 silencing (AGO1-3). These proteins were predicted to preferentially bind to the N and M genomic regions, while being  
220 depleted in the viral UTRs.

221 Lastly, binding of RBPs in cluster 7 and 8 is mostly concentrated in ORF7b as well as E and M protein regions,  
222 respectively. Besides the splicing regulators MBNL1 and SUGP2, cluster 7 contains the ELAVL2 and ELAVL3 RBPs  
223 involved in regulation of RNA stability (38). Previous studies have suggested that ELAVL human proteins might be  
224 affected during infections by the viral RNA that acts as a competitor to tritrate them away from their cellular mRNA  
225 targets (66). While most RBPs in cluster 8 were not found to be functionally related in literature, RBPs KHSRP and  
226 MATR3 have been shown to act as restriction factors in SINV infection (65)

### 227 Predicted RBP binding sites overlap with SECRETE motifs

228 Haimovich et al. (27) recently identified the presence of a unique *cis*-acting RNA element, termed "SECRETE"  
229 motif, which consists of 10 or more consecutive triplet repeats, with a C or a U present at every third base, on the  
230 sequences of both (-) and (+)ssRNA viruses. In context of SARS-CoV-2, a total of 40 SECRETE motifs have been  
231 identified in the viral genome, with a total length of ~1.3 kilobase. This motif has been suggested to be important for  
232 efficient translation and secretion of membrane or ER-associated secreted viral proteins, as well as for viral replication  
233 centers (VRCs) formation. To investigate whether predicted binding sites identified in 2.2 coincide with SECRETE  
234 motifs, we obtained exact locations of all SARS-CoV-2 SECRETE motifs from (27), and subsequently intersected them  
235 with predicted RBP binding sites of all 84 high-quality models containing at least one binding site in SARS-CoV-2.  
236 We observed that a total of 61 RBPs (out of 84) have binding sites overlapping with SECRETE motifs. Further, 30  
237 RBPs with at least 10% of their binding sites overlapping with SECRETE motifs were identified and are termed  
238 'SECRETE-associated RBPs' subsequently. We find that SECRETE-associated RBPs are predominantly found in some  
239 clusters of Figure 3c (cluster 3 and 6-8), while showing an apparent depletion in others (cluster 1-2, Figure 3c). For  
240 instance, 5 (out of 9) SECRETE-associated RBPs (SF3B4, U2AF2, GPKOW, TARDBP and NONO) are found in cluster  
241 6, with TARDBP and NONO being functionally associated to viral regulation (85; 65). Cluster 3 contains 5 (out of 12)  
242 SECRETE-associated RBPs, namely CSTF2, ELAVL4, HNRNPC, PTBP1 and QKI, each associated with multiple  
243 RNA functional processes, including RNA stability, 3'-end formation, splicing and translation (85). Cluster 8 harbors 4  
244 (out of 9) SECRETE-associated RBPs (FUBP3, KHSRP, MATR3 and CPSF6), 3 of which (FUBP3, KHSRP, MATR3)  
245 have 25% or more of their binding sites overlapping with SECRETE motifs. KHSRP is an essential RBP involved in  
246 RNA localization, RNA stability and translation, while METR3 is a regulator of RNA stability. Interestingly, most of  
247 these factors have been previously associated to viral RNA regulation (85). Lastly, all 4 RBPs in cluster 7 (ELAVL2,  
248 ELAVL3, SUGP2 and MBNL1) appear to be strongly associated with SECRETE motifs, as more than 25% of their  
249 respective binding sites are overlapping genomic regions harbouring SECRETE motifs.

### 250 2.3 SARS-CoV-2 variants of concern show gain- and loss-of-binding events

251 Multiple waves of SARS-CoV-2 infections have spread across the globe, some of which resulted in the emergence of  
252 specific lineages of viral variants. The systematic sequencing of thousands of samples from infected patients enabled the  
253 description and categorization of the detected viral sequences, identifying numerous mutations in their sequence when  
254 compared to the initial SARS-CoV-2 reference genome. Some of the thus described strains have been experimentally  
255 characterized as more efficient than others, explaining in part their successful spread at local or global geographic  
256 scales (32; 84; 33). These strains have been defined by the World Health Organization as variants of concern, with  
257 "evidence for increased transmissibility, virulence, and/or decreased diagnostic, therapeutic, or vaccine efficacy" (67).  
258 Specific subsets of mutations have been associated with each variant of concern, when mutations were represented in a  
259 majority of sequenced samples of their lineage. Notably, a special focus has been given with regards to the impact of  
260 mutations occurring within the spike-encoding gene (50), owing its importance in the initial steps of viral infection  
261 and its potential for vaccine neutralization (31). However, due to a lack of appropriate methods, the impact of these  
262 mutations at the regulatory level, such as their impact on protein-RNA interactions, has so far been largely ignored.

## COMPUTATIONAL MAPPING OF THE HUMAN-SARS-CoV-2 PROTEIN-RNA INTERACTOME

263 To fill this gap, we systematically investigated the impact of observed mutations in viral variants of concern on the  
264 predicted binding of RBPs, in order to uncover potential viral hijacking of host proteins directly at the RNA level.

### 265 **A catalog of high-impacting variants across 11 viral strains**

266 We compiled a total of 290 mutations (193 unique mutations, 37 shared across strains) across 11 variants of concern,  
267 including alpha, delta, and omicron strains (Methods 3.11). For each variant and RBP, we evaluated the impact of  
268 the variant in terms of gain- or loss-of-binding by comparing the predicted binding probability of the reference and  
269 alternative allele (Methods 3.11.) Using pysster and DeepRiPe models across 87 RBPs, we obtained a total of 25,230  
270 impact scores, one for each pair of variant and RBP. Notably, three variants (3,037C>T, 14,408C>T, and 23,403A>G)  
271 are consistently found across all viral strains, and their highest absolute delta-scores were respectively associated to  
272 FTO (avg. decrease from 0.474 to 0.356), AQR (avg. decrease from 0.191 to 0.036), and NONO (avg. increase from  
273 0.086 to 0.340). In order to prioritize pairs of variants and RBPs that show a gain- or loss-of-binding, we select a  
274 sub-set of pairs for which either the reference *or* alternative allele pass our binding thresholds (Methods 3.9). Note that  
275 this filter applies a XOR operation, i.e. we are interested in events that lead to either gain- or loss-of-binding (GOB,  
276 LOB). Overall, a total of 315 GOB or LOB events passed the above filter and are depicted in Figure 4a. The majority  
277 of variants introduced small delta in prediction scores, with less than 20% (61) of absolute delta-scores above 0.233  
278 (Figure 4a). As shown in the Supplementary Figure 2a, the top 20% highest-impact variants from Figure 4a accumulate  
279 in different genomic annotations over the SARS-CoV-2 genome. Interestingly, among the RBPs impacted by these  
280 mutations, we find that some strains present multiple high-delta-score mutations for SRSF7 (strains delta, kappa) and  
281 YBX3 (strain lambda), as well as L1RE1, RBPMS, SND1, ZRANB2 (strain omicron) (Supplementary Figure 2b).  
282 Additionally, the omicron strain harbors a particularly large number of variants predicted to impact binding of ORF1  
283 protein (from LINE-1 retrotransposable element).

### 284 **Systematic point-wise *in silico* mutagenesis reveals hypothetical high-impact variants**

285 New viral strains are continuously emerging, some of which are characterized by a faster spread due to newly acquired  
286 sequence variants, highlighting the importance of a continuous monitoring of viral variants which may result in a  
287 selective advantage on the protein or RNA regulatory level. To anticipate and quantify the impact of potentially  
288 unobserved variants, we perform a systematic *in silico* mutagenesis by generating all possible point mutations across  
289 the SARS-CoV-2 genome and score each hypothetical mutation with respect to its impact on RBP binding. Figure 4d  
290 and 4e show exemplary *in silico* mutation tracks for PUM2 and FTO, respectively, with observed reference prediction  
291 scores depicted at the top and the impact of gain- and loss-of-binding variants shown at the bottom. Note that for  
292 visualization purpose, only the delta score of the alternative allele with the highest impact is shown for each position  
293 and RBP. Supplementary Figure 3 shows an impact catalogue of  $29,903 \times 63$  single-nucleotide variants across all  
294 SARS-CoV-2 genome positions and 63 pysster models. The complete set of hypothetical variants together with their  
295 impact scores is available at <https://sc2rbpmap.helmholtz-muenchen.de/>.

### 296 **High-impact sequence variants disrupt known RBP-binding motifs**

297 As *in vivo* RBP-binding is usually driven via the recognition of short sequence motifs, we investigated whether  
298 high-impact variants cause gain or disruption of known binding motifs. To this end, we gathered from each strain  
299 the top 10 variants with highest absolute delta-scores, as illustrated in Figure 4b and 4c for strains alpha and delta,  
300 respectively. This represented a total of 69 unique mutation-RBP pairs, 19 of which were found in more than one  
301 strain. As expected, the majority (54 / 69) of their delta-scores is found to be in the top 1% of the distributions from the  
302 *in silico* mutagenesis. We then computed feature attribution scores (Methods 3.10), centered at the position of each  
303 high-impact variant. Feature attribution maps for the subset of candidate high-impact variants of the alpha and delta  
304 strain are shown in Figure 4b and 4c, respectively. Indeed, we observe that variants with high negative delta score  
305 tend to disrupt known binding motifs of human RBPs. For instance, transition T>G at position 22,917, as seen in the  
306 delta strain (Figure 4c) (as well as in top mutations from epsilon and kappa strains) decreases the prediction score for  
307 PUM2 from 0.795 to 0.158, with only 0.0015% *in silico* variants showing a lower delta-score. As is clearly visible  
308 from the feature attribution analysis (Figure 4c; middle-right), the variant disrupts the well-known PUM2 binding motif  
309 TGTATAT. In a similar manner, transversion A>T at position 23,063 from the alpha strain (Figure 4b; also found in top  
310 mutations from beta, gamma, and mu strains) decreases the prediction score for QKI from 0.488 to 0.049, with 0.006%  
311 *in silico* mutations show a low delta-score. Here, the feature attribution profiles clearly highlight how the known QKI  
312 binding motif ACTAA was detected by the model in the reference sequence, and how the mutation leads to a loss of  
313 this motif. Lastly, the transversion G>C at position 28,280 in the alpha strain (Figure 4b) decreases the prediction score  
314 for FTO binding from 0.679 to 0.209, and only 6 (0.00007%) *in silico* mutations show a delta-score lower than the one  
315 observed (Figure 4d). Although no clear motif is found within the window, the heights of the nucleotides at the position  
316 of the mutation are reduced compared to the reference sequence, reflecting the decreased prediction score.

## COMPUTATIONAL MAPPING OF THE HUMAN-SARS-CoV-2 PROTEIN-RNA INTERACTOME

### 317 **High-impact gain- and loss-of-binding events across viral strains**

318 Among the above set of top 10 highest impact variants per viral strain, we select those that conform to strict gain-or  
319 loss-of-binding (Methods 3.11). We identify a total of 23 (out of 69) change of binding events across 17 variants and  
320 13 RBPs (Table 1). The first example corresponds to a transversion G>T at position 210 in the 5'UTR from the delta  
321 and kappa strains, predicted to induce a loss-of-binding for SRSF7, which we had confirmed from the loss of binding  
322 motif (delta strain heatmap, see Figure 4c). Further, from the ORF1ab gene, two examples of a loss of binding for  
323 RBM20 by the C>T transition at position 3,267 (strain alpha), and a gain of binding of RBM22 from a C>T transition at  
324 position 18,877 (strain mu). From the S gene, a gain of binding is reported for HNRNPC, induced by a C>T transition  
325 at position 21,575 (strain iota), in addition to another gain of binding reported for SF3A3, from a C>A transversion  
326 at position 22,995 (strain omicron). Two mutations occurring in the ORF3a gene are passing our filters for two RBP  
327 impacts: the transition C>T at position 25,469 induces a gain of binding for HNRNPC in delta and kappa strains, while  
328 the G>T transversion at position 25,563 induces a loss of binding for FTO in strains beta, epsilon, iota and mu. Finally,  
329 in the N gene, we report three mutations, two of them impacting FTO binding (one gain in the eta strain, from a deletion  
330 at position 28,278; one loss in the alpha strain, from a G>C transversion at position 28,280), and a loss of binding of  
331 ORF1 protein (from LINE-1 retrotransposable element) in the eta strain, from a A>G transversion at position 28,699.

### 332 **Individual variants impact binding of several RBPs**

333 Among variants that surpass binding-sites thresholds and lead to either gain- or loss-of-binding (Methods 3.11), several  
334 variants impact RBP binding of multiple RBPs simultaneously. For instance, a deletion at position 22,299 (S gene)  
335 identified in the lambda strain, is predicted to induce a gain of binding for ELAVL1, U2AF2, and GPKOW, while  
336 inducing a loss of binding for SF3B4, SF3A3, and MBNL1. Interestingly, all these factors are associated with splicing.  
337 Notably, the MBNL1 loss is also detected in the beta strain, through a deletion happening in a close-by location (at  
338 position 22,281, S gene), suggesting those two mutations may have been retained due to beneficial induction of similar  
339 changes in binding patterns. Another mutation which impacts multiple RBPs is the transition G>A at position 23,048 (S  
340 gene) from the omicron strain, predicted to induce binding of the ORF1 protein from LINE-1 retrotransposable element,  
341 as well as of SND1. Comparably to the MBNL1 impact, two close-by mutations from omicron were associated with a  
342 gain of ORF1 binding (transversion A>C at position 23,013, and transition A>G at position 23,040), further suggesting  
343 joint impact of these mutations on ORF1p binding. The last case of mutations with impact on multiple RBPs concerns a  
344 set of 2 mutations: C>A transversion and C>G transversion at position 23,604, in the S gene. The first is found in alpha  
345 and mu strains, while the second is found in the delta and kappa strains. Both mutations are predicted to induce a gain  
346 of SRSF7 binding, which is visualized for the alpha strain on Figure 4b through feature attribution maps.

### 347 **2.4 RBP-binding across human coronaviruses**

348 While evaluation of impact for reported variants enables the monitoring of potentially functional changes in the SARS-  
349 CoV-2 genome, evaluating changes in binding sites at longer evolutionary time scale might highlight more fundamental  
350 properties of the SARS-CoV-2 virus, as compared to other RNA viruses infecting human. We investigated to which  
351 extent binding sites of human RBPs are conserved across related human coronaviruses. For this purpose, we obtained  
352 genomes and genomic annotations of 6 SARS-CoV-2-related human coronaviruses, namely SARS-CoV-1, MERS,  
353 HCoV-OC43, HCoV-NL63, HCoV-HKU1, HCoV-229E (Methods 3.13). Binding sites were identified in analogy to  
354 SARS-CoV-2 (Methods 3.9) across each viral genome using 87 high-confidence pysster and DeepRiPe models. Figure  
355 5a shows the general binding propensity of RBPs across viral genomes of the 7 coronaviruses. Overall, RBP binding is  
356 conserved across coronaviruses, with the highly pathogenic viruses (SARS-CoV-1, SARS-CoV-2 and MERS) showing  
357 a highly similar binding pattern. Further, a total of 86 (out of 87) RBPs (except FKBP4) were predicted to harbor a  
358 binding site in at least one coronavirus, with only a small variability in the total number of binding RBPs between  
359 individual viruses. However, we observe a greater variability of RBP binding within shared genomic regions across  
360 coronaviruses, for instance in the 5' and 3' untranslated regions (UTRs). Viral UTRs are known to play an important  
361 role in both pro- and anti-viral responses and recent evidence suggests that evolution of the 3' UTR is contributing  
362 to increased viral diversity (15). Indeed, the 3' UTR of SARS-CoV-2 shows a severe truncation when compared to  
363 SARS-CoV-1 and MERS. Given that viral UTRs are not under selective pressure with respect to a translated protein,  
364 they might be more prone to acquire mutations that modulate regulation through host RBPs. Figure 5b and 5c show  
365 RBP binding to the 3' and 5' UTRs across selected coronaviruses, respectively. While SARS-CoV-1, SARS-CoV-2  
366 and MERS show conserved binding on the 5' UTR and cluster closely, a depletion of RBP binding sites is observed in  
367 the 3' UTR of SARS-CoV-2 when compared to SARS-CoV-1 and MERS. To investigate gain-and loss-of-binding in  
368 viral UTRs across the severe pathogenic human coronaviruses SARS-CoV-1, SARS-CoV-2 and MERS, we performed  
369 multiple sequence alignment of the viral 3' and 5' UTRs and compared the predicted binding score profiles across the  
370 three viruses (Methods 3.13).



## COMPUTATIONAL MAPPING OF THE HUMAN-SARS-CoV-2 PROTEIN-RNA INTERACTOME

### 371 **Loss of FXR2-binding in SARS-CoV-2 3' UTR**

372 Figure 5e shows 3' UTR binding of FXR2, a paralog of FMRP (fragile X mental retardation protein). Our model  
373 predicted extensive binding of FXR2 along the 3' UTR of SARS-CoV-1 and MERS, while SARS-CoV-2 showed a  
374 complete lack of predicted FXR2 binding sites, owing to its significantly shorter 3' UTR. On the other hand, Figure 5g  
375 shows that FXR2 binding is conserved in the 5' UTR of SARS-CoV-1 and SARS-CoV-2. FMRP was previously shown  
376 to broadly bind along the entirety the 3' UTR of the Zika virus (ZIKV) (74). However, while FMRP was suggested to  
377 act as a ZIKV restriction factor by blocking viral RNA translation, a significantly reduced ZIKV infection was observed  
378 upon knockdown of FXR2 (74).

### 379 **Conserved FTO binding site in the 3' UTR of SARS-CoV-1 and SARS-CoV-2**

380 Altered expression levels of methyltransferase-like 3 (METTL3) and fat mass and obesity-associated protein (FTO)  
381 have been recently linked to viral replication (99). FTO is a demethylase (eraser) enzyme with enriched binding in the  
382 3' UTR of mRNAs in mammals (58). FTO has previously been suggested as a potential drug target against COVID-19  
383 (97), as targeted knockdown has been shown to significantly decrease SARS-CoV-2 infection (99; 97; 6). Therefore, we  
384 investigated predicted binding of FTO to the 3' UTR of SARS-CoV-2 and related viruses. Indeed, we observed that  
385 SARS-CoV-1, SARS-CoV-2 and MERS, as well as the less pathogenic viruses HCoV-HKU1 and HCoV-OC43 harbor  
386 at least one FTO binding site in their 3' UTR (Figure 5b). Further, Figure 5d shows that while SARS-CoV-1 and MERS  
387 harbor multiple shared FTO binding sites along their 5' UTR, SARS-CoV-2 only harbors one FTO binding site at the 3'  
388 end of its 5' UTR which is exclusively shared with SARS-CoV-1.

### 389 **Newly acquired TARDBP binding in the SARS-Cov-2 5' UTR**

390 We next focus on TARDBP (also known as TDP-43) (Figure 5f), which was predicted to bind the 5' UTR of a  
391 SARS-CoV-2 mutant in a recent study (60). TARDBP, a host protein implicated in pre-mRNA alternative splicing, has  
392 been shown to play a role in viral replication and pathogenesis in the context of coxsackievirus B3 infection (42). In  
393 contrast to the findings of Mukherjee et al. (60), our model identified a TARDBP binding site at the genomic range of  
394 89-98 in the wild-type reference of SARS-CoV-2. Interestingly, in addition to observing a lack of predicted binding  
395 signal of TARDBP on the 5' UTR of SARS-CoV-1 and MERS, we found a complete lack of TARDBP binding to the 5'  
396 UTR of any of the other investigated coronaviruses (Figure 5c). This suggests that 5' UTR TARDBP binding potential  
397 is newly acquired in SARS-CoV-2 and may affect its virulence.

## 398 **2.5 A functional catalog of human RBPs with predicted SARS-CoV-2 interaction**

399 To understand the functional impact of RBPs on the SARS-CoV-2-mediated COVID-19 disease, we set out to interrogate  
400 the breadth of publicly available OMIC research, thereby gathering supportive evidences for our 87 RBPs models  
401 (Figure 6). To this end, we collected 97 data sets of experimental research results from 22 studies (Methods 3.15)  
402 covering experimentally determined and predicted viral RNA - host RBP interactions as well as multi-level (OMICS)  
403 data related to SARS-CoV-2 cell line infections, shedding light on viral entry, protein-protein interactions and host cell  
404 regulation. Studies which are closer to disease phenotypes, like CRISPR cell survival assays and COVID-19 patient  
405 data, were also included. In addition, we collected evidence of direct involvement of RBPs in SARS-CoV-2 infection,  
406 as reported in the SIGNOR database, a manually curated resource of pathways and genes involved in SARS-CoV-2  
407 (49). All data sets were harmonized and integrated through the use of knowing01 (kno) software to annotate RBPs by  
408 automated mapping of gene, variant and protein identifiers, yielding reported evidence of binding or regulation for 85  
409 out of 87 (97.7%) RBPs models.

410 We found that a large fraction (63 out of 87, 72.4%) of RBPs were identified to directly bind SARS-CoV-2 RNA  
411 using affinity-purification methods (69; 18) (Figure 6), validating the interaction of these RBPs with the viral RNA.  
412 Interestingly, only 32 out of 87 RBPs (36.8%) have previously had reported binding sites profiles over the SARS-CoV-2  
413 genome by related methods catRAPID (87) or PRISMNet (80). We thus complement the knowledge on binding site  
414 locations over SARS-CoV-2 RNA with 55 RBPs uniquely explored by our framework, 36 of which are experimentally  
415 supported for viral RNA interactions (labeled as 'NOVEL validated', Figure 6). Our holistic comparison revealed  
416 that the majority of explored RBPs (75, 86.2%) were previously reported to be part of host-pathogen PPI networks  
417 and cellular pathways which are altered during infection by either SARS-CoV-2, SARS-CoV-1 or both (Figure 6). In  
418 addition, 34 out of the 87 (39.1%) were identified as essential genes in CRISPR knock-out screenings, highlighting the  
419 importance of RBPs in the infection process, immune response and viral replication, through direct interaction with  
420 the viral genome. Although no RBP co-localizes with loci associated to COVID-19 severe disease courses (GWAS)  
421 under genome-wide significance, we identified 44 (50.6%) RBPs with nominal significance. When considering the  
422 total of 2,730 coding genes co-localizing nominally associated loci, this represents a significant enrichment for RBPs

## COMPUTATIONAL MAPPING OF THE HUMAN-SARS-CoV-2 PROTEIN-RNA INTERACTOME

423 (odds ratio of 7.8, Fisher test p-value  $<2.2e-16$ ), suggesting their importance in patient's course. Finally, a small set  
424 of our predicted-binding RBPs was shown to be supported only from CRISPR screens or found deregulated across  
425 COVID-19 patients, without evidence of viral RNA binding from previous studies, neither functional evidence in  
426 molecular networks altered by SARS-CoV-2 infection (labeled as 'NOVEL & disease relevant', Figure 6). Taken  
427 together, the large overlap between the RBPs we selected and the different resources considered confirms that hijacking  
428 host RBPs is crucial to the infection life cycle of the virus, through the direct binding of these RBPs to the viral genome  
429 only or in combination with host-pathogen protein-protein interactions.

### 430 **3 Material and Methods**

#### 431 **3.1 ENCODE data and preprocessing**

432 Enhanced CLIP (eCLIP) datasets were obtained from the ENCODE project database, which comprises 223 eCLIP  
433 experiments of 150 RBPs across two cell lines, HepG2 and K562. For RBPs with experiments in both cell lines, we  
434 selected only data of eCLIP experiments from the HepG2 cell line for downstream analysis, as those were demonstrated  
435 to yield higher performing models (compared to K562) in previous studies (5). Narrow peaks of each eCLIP library  
436 were taken directly from ENCODE and preprocessing was performed as follows: for each of the two replicates of a  
437 given eCLIP experiment, peaks were first intersected with mRNA locations obtained from the GENCODE database  
438 (Release 35) and only overlapping peaks were retained. Next, the 5'-end of each peak was defined as the cross-linked  
439 site, as it usually corresponds to the highest accumulation of reverse transcription truncation events. A 400bp window  
440 was then centered around the cross-linked site for each peak, defining the input window of the downstream model.  
441 Input windows of both replicates were intersected reciprocally with a required overlap fraction of 0.75, ensuring that  
442 only those peaks which are present in both replicates are considered for downstream training set construction. Finally,  
443 the top most 50,000 windows with a read-start count FC of 2.0 above the control (SMInput) experiment were selected  
444 for each RBP.

#### 445 **3.2 Pysster training set construction**

446 For each RBP, a classification dataset of bound (positive) and unbound (negative) RNA sequences was constructed.  
447 Positive samples were obtained by taking corresponding 400nt peak-region windows from the previous step (3.1), while  
448 two distinct sets of negative samples were generated. First, 400nt long regions which did not overlap with binding sites  
449 of the given RBP were sampled from transcripts harboring at least one binding site. This constraint ensures that the  
450 transcript is expressed in the experimental cell type and would not be observed as RBP-binding in other cell types. The  
451 second set of negative samples was generated by randomly sampling binding sites of other RBPs. This ensures that  
452 any CLIP-seq biases (such as U-bias during UV-C cross-linking (79), (93)) are present in both positive and negative  
453 samples and prevents the model from performing a biases-based sample discrimination during the training. Together,  
454 this yields a three-class training set, where class 1 corresponds to positive samples and class 2 and 3 correspond to  
455 negative samples. Samples of class 2 and 3 were sampled at a 3:1 ratio with respect to class 1. Finally, generated  
456 samples were randomly split into train, validation and test sets at a ratio of 70:15:15, respectively.

#### 457 **3.3 Pysster model**

458 The *pysster* Python library (5) was used for implementation of the model which consists of three subsequent one-  
459 dimensional convolutional layers, each with 150 filters of size 18, followed by a single fully connected layer with 100  
460 units. The ReLU activation function is applied to each intermediate layer output and a maximum pooling layer is added  
461 after every convolutional layer. Finally, a fully connected layer with 3 units, one for each of the three output classes, is  
462 added. Dropout (75) with a rate of 0.25 was applied to each layer, except for input and output layers. The model was  
463 trained with the Adam optimizer (41) using a batch size of 512 and a learning rate of 0.001. For each RBP, we trained  
464 for at most 500 epochs and stopped training in case the validation loss did not improve within the last 10 epochs.

#### 465 **3.4 Pysster binary classification threshold**

466 As *pysster* models are trained as a 3-class classification problem with class imbalance, we re-calibrate each model for  
467 the binary classification task by introducing a binary decision threshold  $t_m$  on the predicted positive-class probability  
468 scores. For each model  $m$ ,  $t_m$  is defined as the threshold which maximizes the F1 performance (Section 3.7.1) of  
469 the model with respect to bound vs. unbound binary classification obtained by pooling class 2 and 3 samples into a  
470 common 'unbound' class. This threshold is used to identify bound regions in the viral sequence (Section 3.9).

#### 471 **3.5 DeepRiPe model**

472 We obtained pre-trained DeepRiPe models from Ghanbari et al. (23) and retained models for 33 out of the 59 RBPs,  
473 filtering out models where no informative sequence motif could be learned by the model. The PAR-CLIP-based models  
474 used in this study are modified versions of the DeepRiPe neural network, where only the sequence module to extract  
475 features from the RNA sequence is used. Briefly, the model consists of two convolutional layers, one fully connected  
476 layer and one output layer that contains  $k$  sigmoid neurons to predict the probability of binding, one for each RBP. Each  
477 convolutional layer has a rectified linear unit (ReLU) activation, followed by a max pool layer and a dropout layer  
478 with probability of 0.25. 90 filters with length 7 and 100 filters of length 5 for the first and second convolution layers,

## COMPUTATIONAL MAPPING OF THE HUMAN-SARS-COV-2 PROTEIN-RNA INTERACTOME

479 respectively. The fully connected layer has 250 hidden units and a ReLU activation. Details in data preparation and  
480 model training are outlined in Ghanbari et al. (23).

### 481 3.6 Single-nucleotide predictions

482 The pysster and DeepRiPe positive-class prediction score corresponds to the probability that input RNA sequence is  
483 bound by the RBP of interest. By design, this score is assigned to the entire input sequence, although RBP binding  
484 sites are much more local, usually spanning only a few nucleotides (14). To obtain single-nucleotide binding site  
485 probabilities from both pysster and DeepRiPe models along an RNA sequence, we employ a one-step sliding-window  
486 approach to scan over a given RNA sequence, where the predicted positive-class probability score is assigned to the  
487 center nucleotide of the input window. In order to obtain predictions over the entire RNA sequence, the 5' and 3'  
488 sequence ends are 0-padded.

### 489 3.7 Pysster performance evaluation and model selection

#### 490 3.7.1 Precision-recall and F1 performance

491 As the validation loss was monitored for the purpose of early-stopping, the precision-recall (PR) and F1-score  
492 performance of the pysster models was evaluated on the test set. Models with an area under the PR curve (auPRC) of  
493 less than or equal to 0.6 were deemed poor quality and thus excluded from the downstream analysis.

#### 494 3.7.2 Performance in practice

495 Training datasets are sampled at a fixed positive-negative ratio which hardly reflects the ratio of bound and unbound sites  
496 of RNA transcripts found *in vivo*. In practice we expect that for some transcripts regions, binding sites of a particular  
497 RBP are not observed over several kilo-bases, while other regions, such as 5' and 3' untranslated regions (UTRs), might  
498 harbor a dense clustering of binding sites. To measure the ability of pysster models to accurately predict *de novo* RBP  
499 binding-sites along whole-length RNA transcripts, we introduce the concept of Performance-In-Practice (PIP), which  
500 measures how well the single-nucleotide prediction score of the model correlates with binding sites identified by eCLIP.  
501 For a given RNA sequence, the PIP of a model is defined as the Spearman correlation coefficient (SCC) between the  
502 truncated prediction scores  $p_i^{trunc}$  and a binary vector obtained by labeling all positions that fall within eCLIP binding  
503 sites with 1 and 0 otherwise. Here,  $p_i^{trunc}$  refers to a modified version of the prediction score  $p_i$  defined as

$$p_i^{trunc} = \begin{cases} p_i, & \text{if } p_i \geq t_m \\ 0, & \text{otherwise} \end{cases}$$

504 where  $t_m$  is a threshold obtained for each model as outlined in Section 3.4. For each model, we perform extensive PIP  
505 analysis on the human transcriptome as follows. First, we select the set of transcripts which contain at least one binding  
506 site for it. From this set, we uniformly draw 100 transcripts without replacement as hold-out transcripts. Subsequently,  
507 we intersect positive and negative training samples with the hold-out transcripts and discard all samples that overlap  
508 with any of the hold-out transcripts before retraining pysster on the remaining training samples. We use the resulting  
509 models to predict along the hold-out transcripts as described in Section 3.6 and compute the PIP score for each hold-out  
510 transcript. Finally, models with a median PIP score of less than or equal to 0.1 were excluded from downstream analysis.

### 511 3.8 Estimating significance of prediction scores

512 To directly control the false positive rate of binding site prediction from both pysster and DeepRiPe models on the  
513 viral genome, we estimate prediction score significance via an RNA sequence permutation test. In order to obtain a  
514 null-distribution of predictions (positive-class) scores, we first compute the di-nucleotide frequencies on the viral RNA.  
515 Next, we perform frequency-weighted sampling of di-nucleotides to construct a set of  $N = 10,000$  null-distributed  
516 inputs. Null-distributed prediction scores for each model are then obtained by predicting on those sequences. A p-value  
517 is assigned to each observed prediction score  $p_i$  in the viral sequence by computing the fraction of scores from the null  
518 distribution  $p_j^{null}$  for which  $p_j^{null} > p_i$ ,  $j = 1, \dots, N$ .

### 519 3.9 Identifying RBP binding sites

520 We identify RBP binding sites on the viral RNA sequence using predicted single-nucleotide binding probabilities  
521 (Section 3.6) together with estimated p-values (Section 3.8). For each pysster model, we classify nucleotides in the viral  
522 RNA as "bound" if the predicted probability score is equal or greater than the estimated binary threshold  $t_m$  (Section

## COMPUTATIONAL MAPPING OF THE HUMAN-SARS-CoV-2 PROTEIN-RNA INTERACTOME

523 3.4) and the score is found to be significant ( $p < 0.01$ ). Regions with a consecutive stretch of bound nucleotides of  
524 at least length 2 are then defined as a RBP binding site. Neighboring binding sites that are spaced by less than 10  
525 nucleotides are merged to a single binding site. Note that for DeepRiPe models, nucleotides in the viral RNA are  
526 considered "bound" if the probability score is found to be significant ( $p < 0.01$ ) and no score threshold is applied.

### 527 3.10 Base-wise feature attribution via Integrated Gradients

528 To gain insight into which RNA sub-sequences are driving factors for RBP binding, we compute sequence importance  
529 scores using Integrated Gradients (IGs) (81; 23). Starting from an input baseline, IG performs a step-wise linear path  
530 interpolation between the baseline and the actual input sequence and computes the gradients of the interpolated inputs  
531 with respect to an output neuron. That is, we obtain a vector of importance scores over the input sequence which  
532 indicate which nucleotides of the input contributed most toward the prediction. Here, we choose the 0-vector (i.e. the  
533 one-hot encoding of all nucleotides is set to 0) as the baseline and perform 50 baseline-input interpolation steps. To  
534 obtain sequence importance scores for a given binding site, we compute IGs with respect to an input window centered  
535 around the binding site. For sequence-motif construction, the heights of nucleotides in the input sequence is given by  
536 the feature attribution weights.

### 537 3.11 Analyzing mutations in variants of concern

538 Variant information of 11 SARS-CoV-2 viral variants (alpha, beta, delta, epsilon, eta, gamma, iota, kappa, lambda,  
539 mu, omicron) was obtained from the UCSC genome-browser for the SARS-CoV-2 virus (17), and converted into VCF  
540 format. For each strain, we first created a 'mutated' strain-specific genome, using the viral reference sequence and the  
541 set of strain-defining variants. We then center a window at the reference position of each genomic variant and extract  
542 the mutated sequence for subsequent prediction via each model. We note that for cases where genomic variants are  
543 in close proximity with each other, extracted windows might contain multiple mutations. This is crucial, as only the  
544 combination of multiple variants might lead to gain or loss of RBP binding. The resulting prediction score on each  
545 alternative allele (ALT) is then compared with the prediction score of the same window on the reference sequence  
546 (REF). To quantify the impact of each mutation, we compute a *delta* score between the prediction score of ALT and  
547 REF sequence:

$$\Delta_{score} = score_{ALT} - score_{REF}. \quad (1)$$

548 Mutations with a positive delta score sign represent 'gain-of-binding' (GOB) events, while mutations with negative sign  
549 represent 'loss-of-binding' (LOB) events. To further narrow down the set of mutations, we compile a subset of mutation  
550 that lead to a gain- or loss-of-binding (GOB and LOB), defined as instances where (in case of LOB) the REF score  
551 is passing the binding site score threshold and p-value (Sections 3.4 and 3.8) while the ALT does not, or vice versa  
552 (in case of gain of binding). As for binding site calling (Section 3.9), we use a significance level of 0.01 as p-value  
553 threshold for both pysster and DeepRiPe models.

### 554 3.12 *In silico* mutagenesis

555 We perform *in silico* probing of the effects of all possible point-mutations on RBP binding across the SARS-CoV-  
556 2 genome. At each viral genome position, the reference base was mutated to each of the three alternative bases.  
557 Subsequently, prediction was performed on the input windows derived from each ALT allele using all high-quality  
558 pysster models. Finally, as described in Section 3.11, an impact score is computed and a set of change-of-binding  
559 mutations is compiled.

### 560 3.13 Comparative analysis of human coronaviruses

561 Besides SARS-CoV-2, we obtained reference sequences for 6 other human coronaviruses, including SARS-CoV-1,  
562 MERS, HCoV-229E, HCoV-HKU1, HCoV-NL63 and HCoV-OC43 from NCBI (68). Using high-quality models from  
563 both pysster and DeepRiPe (Section 3.7), we perform single-nucleotide binding prediction along each viral RNAs  
564 (Section 3.6). Next we compute prediction empirical p-values for each viral sequence (Section 3.8) by generating a  
565 dedicated null distribution of scores for each virus and RBP. RBP binding sites across viruses were then identified as  
566 described in Section 3.9. We evaluate genomic-element preference across a subset of shared viral genomic locations  
567 (ORF1ab, E, N, M, S, 5' UTR, 3' UTR) for each RBP and virus by intersecting the predicted set of binding sites of  
568 each virus with its RefSeq annotations. To compute multiple sequence alignments (MSA) between genomic elements  
569 of betacoronaviruses, we use the ClustalO (72) algorithm with default parameters.

## COMPUTATIONAL MAPPING OF THE HUMAN-SARS-CoV-2 PROTEIN-RNA INTERACTOME

### 570 **3.14 Functional annotation of RBPs**

571 To assess the potential role of RBPs with predicted binding on viral RNA sequences, we manually curated all RNA-  
572 related functions of the 87 RBPs with good predictive models using the GeneCards, Uniprot and RBP2GO databases  
573 (77).

### 574 **3.15 Public COVID-19/coronaviruses OMICS data**

575 To assess regulatory information of RBPs across available coronavirus/COVID-19 multiOMICS data, we downloaded  
576 evidence from 22 studies. We imported study-relevant supplementary tables via knowing01, which harmonizes data  
577 tables and links results to molecular information, like human gene symbols, UniProt identifier, variant positions as  
578 available in the proprietary CellMap unified data model (Version 2022/03). A list of 87 RBPs with good model  
579 performance were loaded as list of Gene Symbols. To ensure that all RBP human gene symbols are identically named  
580 in African Green Monkey OMICS data, we used VeroE6 cells linked to human symbols.

581 A total of 97 research results were grouped into the following study types:

- 582 • extended interactomes from experimental determined of host RBP-SARS-CoV-2 interactions using affinity  
583 purification and mass spectrometry (18; 69; 89)
- 584 • computational predictions of host RBPs- SARS-CoV-2 interactions in the 5' UTR, 3' UTR and Spike S  
585 genomic region of the viral RNA with either catRAPIDomics (87) or the PRISMNet tool (80)
- 586 • viral-host protein-protein interactions (PPIs) measured by affinity-purification followed by mass spectrometry  
587 (24; 78)] and yeast two hybrid screenings (40)
- 588 • multiOMICS data, including the regulation of the host proteomics, phosphoproteomics, ubiquitinomics and  
589 transcriptomics up to 24 hours after coronavirus infection (4; 78), as well as the effectome, which includes  
590 deregulated host proteins 72 hours after SARS-CoV-2 induced expression of each of the viral proteins (78)
- 591 • CRISPR phenotype screens probing cell survival few days after viral infection with single genes knockouts in  
592 human (24; 30; 70; 91) or African green monkey [(92)] cell lines
- 593 • genome-wide association studies (GWAS) linking human genetic variation to COVID-19 disease severity (64)
- 594 • patient OMICS data, including proteomics and transcriptomics regulation of whole blood, serum or plasma of  
595 mostly inpatients (10; 12; 13; 22; 57; 63; 71; 95)

596 To filter for significant regulation in each data set, we applied significance cutoffs per study result. We chose to select  
597 two different significance levels to get lists of regulation with a stringent (adjusted p-value < 0.01) and a lax (adjusted  
598 p-value < 0.1) cutoff threshold, whenever available. Few data sets only provided raw p-values for which we used  
599 with lower cutoffs. Patient transcriptomics data were used with much lower cutoffs, due to the inflation of regulated  
600 genes on typical cutoffs. For GWAS data we employed a genome-wide (p-value < 5e-08) and nominal (p-value <  
601 0.01) significance cutoff, for stringent and lax cutoffs, respectively. Finally we annotated all 87 RPBs with regulated  
602 molecules via the knowing01 Annotate feature and visualized the number of evidences of RBPs in each data set in a  
603 count matrix.

## 604 4 Discussion

605 Strong evidence suggests that human RBPs are critical host factors for viral infection by SARS-CoV-2, yet there is no  
606 feasible experimental approach to map exact binding sites of RBPs across the SARS-CoV-2 genome systematically. To  
607 combat this knowledge gap, we constructed the first *in silico* human-virus RBP-RNA interaction map for SARS-CoV-2  
608 using predictions from pysster (5) and DeepRiPe (23) models trained on a large cohort of eCLIP and PAR-CLIP  
609 datasets, respectively. The use of high-capacity CNN classifiers represents a significant improvement over previous  
610 computational studies performing motif scanning over the SARS-CoV-2 genome (75; 3), as it enables the learning  
611 of more complex binding syntax and thus the detection of binding sites for RBPs with no cleanly defined sequence  
612 motif. This is evident by the fact that we observed high performance for RBPs without annotations of binding motifs  
613 in literature. On the other hand, we demonstrated that deep learning methods are by no means black boxes, as we  
614 recovered known binding motifs for several RBPs (including QKI, RBFOX2 and TARDBP) using gradient-based  
615 attribution methods. Together with stringent performance evaluation and conservative selection of high-quality models,  
616 these results suggest that our predictions represent bona fide binding sites. In a recent study, the PRISMNet deep  
617 learning model was used to infer binding of 42 host RBPs to the SARS-CoV-2 genome (80). However, predicted  
618 binding sites by PRISMNet are restricted to the 5' and 3' viral UTR regions are rather large, with some spanning over  
619 hundreds of nucleotides, while RBP binding usually only occurs across short stretches of RNA *in vivo*. In contrast, our  
620 approach generated single-nucleotide binding probabilities across the entire viral genome and may therefore yield a  
621 more complete picture of the binding landscape of human RBPs to SARS-CoV-2.

622 Our study identified known, as well as novel human RBPs to interact with SARS-CoV-2 (Figure 6). Further, the  
623 generated binding map provides a rich resource for future functional studies, in particular for investigating the role of  
624 the SARS-CoV-2 protein-RNA interactome in context of the viral life cycle. For instance, binding site predictions may  
625 be used to accelerate the discovery of host RBPs that engage in both pro- and anti-viral functions by directly interacting  
626 with the viral RNA. Further, predictions may aid in the identification of functional sites on the viral RNA that can  
627 be therapeutically targeted by RNA drugs, such as anti-sense oligonucleotides, to interfere with host RBP binding.  
628 In addition to constructing a RBP binding map on the SARS-CoV-2 reference sequence, we quantified the impact of  
629 sequence variant from 11 SARS-CoV-2 strains, including the alpha, delta and omicron viral strains.

630 Additionally, we applied a systematic *in silico* mutagenesis of all positions in the SARS-CoV-2 genome, pinpointing  
631 mutations associated with particularly high impact, which could represent potential high-risk variants to monitor in  
632 the future. Our analyses confirmed that our models can effectively be used to identify mutations with high-impact  
633 potential using the prediction scores, either for mutations observed in viral variants of concern (Figure 4a) or from *in*  
634 *silico* mutagenesis (Supplementary Figure 3). Such mutations can be evaluated further through the computation of  
635 attribution maps, highlighting important nucleotide in a given window of interest, and how their importance is impacted  
636 by the mutation. In previous studies variants of concerns have been prioritized through their potential impact on the  
637 sequence of viral proteins, in particular the Spike protein. Our results complement these findings, and enable to better  
638 understand the efficiency of specific lineages of SARS-CoV-2 in the context of RBP-viral RNA interactions, providing  
639 with a map of mutations of high potential for hijacking important host RBPs, or on the contrary evade binding of  
640 anti-viral RBPs. With our comparative analysis of RBP-RNA interactions across seven coronaviruses we contribute to  
641 the identification of genomic features and factors which confer unique characteristics to SARS-CoV-2 transmission  
642 and pathogenicity, compared to SARS-CoV-1, MERS, and less pathogenic coronaviruses. Both variants of concern  
643 and comparative analysis highlight gain- or loss-of-binding affecting host RBP-viral interactions and therefore pinpoint  
644 RBPs which can be prioritized for further screening.

645 We integrated knowledge of our predicted RBPs across other pathogens, host-viral protein-protein interactions, numerous  
646 studies collecting functional and phenotypic data, such as GWAS and CRISPR screens, as well as multi-omics COVID-  
647 19 patient data, in order to pinpoint RBPs with clinical significance. By this analysis, we mainly identify five sets  
648 of RBPs predicted to interact with the SARS-CoV-2 genome. The first set comprises core RBP predictions with  
649 numerous independent evidences in the scientific literature of their involvement in regulation of viral infection, included  
650 SARS-CoV-2. Proteins in this core set are confirmed by additional *in silico* methods, as well as experimental assays  
651 to bind SARS-CoV-2, and identified as deregulated or affected in multi-omics studies and/or CRISPR, GWAS and  
652 patient data of SARS-CoV-2 infection. Among them, we find several known regulators of viral processes, such as the  
653 hnRNPR viral restriction factors (65), the IGF2BP1-3 RBPs, which are mainly ubiquitinated during SARS-CoV-2  
654 infection (78) and linked, through GWAS, to poor disease outcome (34), as well as key regulators of SARS-CoV-2  
655 infections such as the stress granules-associated RBPs CAPRIN1 and KHDRBS1 (37), associated to pathways such  
656 as ER stress, Inflammation, cytokine storm and others (Supplementary Table 3), the pro-viral DDX3X factor (9) and  
657 the host factor NONO (65), previously shown to promote innate immune activation in HIV infection (44). Important  
658 regulators of mRNA splicing (QKI, PTBP1 and U2AF2), and other processes (TARDBP, TIAL1) are also part of this

## COMPUTATIONAL MAPPING OF THE HUMAN-SARS-CoV-2 PROTEIN-RNA INTERACTOME

659 group of RBPs. Notably, many of the RBPs we highlighted throughout our binding site analysis on the SARS-Cov-2  
660 genome, impacts from mutations in viral variants, or comparative genomic changes of binding sites fall into this group.  
661 For instance, TARDBP and QKI are two RBPs that are well supported, in particular through experimental identification  
662 of their binding to the viral RNA, in addition to OMICs support and CRISPR (TARDBP) or GWAS (QKI). We also  
663 identify TARDBP as a particularly important RBP in the context of SARS-CoV-2 infection due to the prediction of a  
664 unique binding site in the virus 5' UTR, when compared to SARS-CoV-1, MERS and other coronaviruses. A second  
665 set of RBPs comprises 36 proteins uniquely predicted by our framework as binders of SARS-CoV-2, which harbour  
666 experimental extensive support.

667 An example of RBP of interest in this group is the Serine/arginine-rich splicing factor 7 (SRSF7). Previous studies  
668 have shown that SRSF7 interacts with coronavirus RNA (76). It has also been suggested that this spliceosome protein  
669 could be sequestered by the viral genome, the later thus acting as a sponge through these putative binding sites, to alter  
670 host splicing processes. Among the high-impact mutations in the SRSF7 gene position 23,604 (S protein gene) is found  
671 mutated across multiple strains, with different alternative nucleotides: a C>A transversion is found in alpha and mu  
672 variants, while a C>G transversion is found in delta and kappa variants. Both mutations are associated to a positive  
673 delta score, therefore a gain of binding. This position has been suggested by previous studies to be a major driver of the  
674 increased infection efficiency of these viral variant, as a modifier of the S protein sequence (P680R) (52), although  
675 additional studies indicate that other mutations may be required for an actual effect ((53; 98)). The gain of binding we  
676 identify here could also suggest that the translation of the S gene into the protein is improved through the recognition of  
677 the newly created binding site by SRSF7.

678 Besides SRSF7, the large number of binding sites for splicing factors at the 5' UTR of the SARS-CoV-2 (cluster 6,  
679 Figure 3c) and the pervasive binding of several host and viral restriction factors (cluster 4, Figure 3c) suggests that  
680 these RBPs are likely to get sponged on the viral genome and by that modulate post-transcriptional regulatory networks  
681 in the host cell.

682  
683 One other interesting RBP in this group is represented by FXR2, paralog of FXR1 and FMR1 which are identified  
684 as direct binders of SARS-CoV-2 (Figure 6). Recent evidence suggests that FXR2 selectively interact with MERS viral  
685 proteins but not with viral proteins from SARS-CoV-1 and SARS-CoV-2 [(24)]. While we find evidence of FXR2  
686 binding along the SARS-CoV-2 genome, this is in agreement with the results of our comparative analysis with other  
687 human coronaviruses, where we observe extensive binding of FXR2 along the 3' UTR of SARS-CoV-1 and MERS, but  
688 depletion of FXR2 binding in the SARS-CoV-2 3' UTR. Together with the evidence of genetic association of FXR2 to  
689 COVID-19 disease severity (35) our findings suggest a fine-tuning role of FXR2 in regulating the severity of the infection.

690  
691 From these two sets, we can also highlight many RBPs with functions related to endoplasmic reticulum processes.  
692 SARS-Cov-2 utilizes the endoplasmic reticulum (ER)-derived double membrane vesicles (DMVs) as replication centers.  
693 RNA viruses, included SARS-CoV-2, contains several instances of an RNA regulatory motif, called SECRETE motif  
694 (27) which facilitates localization to the ER and increases viral protein translation, as well as viral replication. Such  
695 motif is also found in some human mRNAs encoding for proteins involved in innate immunity and associated with  
696 epithelial layers targeted by SARS-CoV-2. This suggests that host and pathogen might compete for ER-associated  
697 RBPs and this might make the host more vulnerable to the infection. Among our validated RBPs in set 1 and 2 (Figure  
698 6) we identified several SECRETE-associated RBPs, defined as those proteins where more than one fourth of their  
699 predicted binding sites overlapped instances of the SECRETE motif on the SARS-CoV-2 genome. These include  
700 FUBP3, KHSRP and MATR3, already identified previously as important host or restriction factors for other RNA  
701 virus infections (65). Interestingly, we linked MATR3 to several CRISPR studies showing that this factor is essential  
702 for SARS-CoV-2 replication, as well as to many nominal variants in all GWAS data (Figure 6). MATR3 physically  
703 interacts with G3BP1, another predicted RBP in this set which been found to interact specifically with SARS-CoV-2  
704 nucleocapsid (N) protein, control viral replication and localize (together with MATR3) at stress granules where G3BP3  
705 is taken away from its typical interactions partners (62). Our and previous data (Figure 3) suggest that direct binding of  
706 G3BP3 and MATR3 to the SARS-CoV-2 RNA could constitute an additional mechanism used by the virus to interfere  
707 with the G3BP3-MATR3 PPI network and impair stress granule formation. The fact that G3BP3 binding is enriched in  
708 correspondence of the gene encoding for protein N (Figure 3c) might also suggest a direct regulation of this transcript  
709 by this RBP in a sort of feedback loop manner.

710  
711 The other three sets of RBPs predicted to bind SARS-CoV-2 correspond to 1) proteins with *in silico* support from  
712 other predictive tools, but no experimental validation of direct binding to SARS-CoV-2 (named 'Predicted only');  
713 2) novel candidate SARS-CoV-2 binders, uniquely predicted by our method, no experimental validation but large  
714 functional support from host-pathogen PPI, CRISPR and patient omics data (named 'Novel infection relevant'), and 3)  
715 putative novel regulators that lack so far functional evidence across studies but were nonetheless found to be deregulated



## COMPUTATIONAL MAPPING OF THE HUMAN-SARS-CoV-2 PROTEIN-RNA INTERACTOME

716 in COVID-19 patients (named 'Novel disease relevant'). The fat mass and obesity-associated protein (FTO) is an  
717 example of a newly identified regulatory RBP for SARS-CoV-2. FTO is a demethylase (19), and while it has been  
718 suggested that the virus could hijack the host epigenome [(2)], a recent study showed that the viral genome itself  
719 was methylated (51), with a negative effect on viral replication efficiency. Besides the predicted binding pattern,  
720 FTO also presented numerous important gain-or loss-of-binding across many viral strains. Although there was no  
721 clear trend towards systematic loss of binding of FTO across the viral variants, we were able to point out multiple  
722 close-by mutations in the alpha variant that were associated to a significant loss, around the position 28,280 (Figure 4b).  
723 Finally, the FTO protein was identified as key risk factor for obesity, which is also a known risk for COVID-19 severity.  
724 FTO coding region harbored also nominal genetic associations to COVID-19 severity (variant lowest p-value 0.0053).  
725 Interestingly, FTO was additionally found to be significantly regulated on gene level in blood serum of patients admitted  
726 to ICU care (adj. p-value 7.72E-06) (63). A small set of novel predicted RBPs, with little to no experimental evidence  
727 across multiple functional studies, includes the ELAVL2-4 factors, the DND1 RBP and the splicing factors SRRM4  
728 and SF3A3 (Figure 6). Interestingly, ELAVL2-4 RBPs, found in our analysis to be SECRete motif-associated RBPs,  
729 and SRRM4 RBP are neuron-specific proteins and were found, through our integrative analysis, to be deregulated in  
730 COVID-19 patients. This points to novel promising candidates whose molecular mechanisms can be further investigated  
731 experimentally.

## 732 5 Conclusion

733 Viruses depend on essential host factors at all stages of their infection cycle. One family of host factors, RNA-binding  
734 proteins (RBPs), are involved in multiple aspects of post-transcriptional regulation and are characterized by their ability  
735 to bind to short RNA motifs. While several RBPs have been associated with SARS-CoV-2, some of which may represent  
736 drug-able targets for anti-viral therapy, cost and time constraints render a comprehensive experimental profiling of  
737 human RBPs to the SARS-CoV-2 RNA infeasible. To fill this knowledge gap, we instead identified binding of human  
738 RBPs to the SARS-CoV-2 genome computationally. Here, we used the pysster and DeepRiPe frameworks together with  
739 data from over 200 eCLIP and PAR-CLIP experiments to train RBP binding site predictors on the basis of convolutional  
740 neural networks (CNN). By applying stringent performance filters, we obtained a set of high-quality prediction models  
741 for 88 RBPs and created an *in silico* binding map of human RBPs along the SARS-CoV-2 genome at single-nucleotide  
742 resolution. Predicted binding profiles of RBPs suggested that groups of RBPs exhibit similar binding patterns on the  
743 viral genome and that RBPs within these group may be functionally related, for example, by being associated to the  
744 SECRETE motif important for efficient viral replication. We identify RBPs with clinical relevance, by analyzing our  
745 data in the context of functional and clinical studies, including genetic screens and COVID-19 patient data. We further  
746 utilized trained models to score the impact of strain-defining sequence variants across 11 SARS-CoV-2 strains. Several  
747 variants that result gain or loss of RBP-binding were identified, some of which simultaneously impact the binding of  
748 multiple RBPs or which are conserved in multiple viral strain. In addition to the analysis of observed variants, we  
749 quantified the impact of hypothetical variants by performing extensive *in silico* mutagenesis, generating all possible  
750 point mutations across the SARS-CoV-2 genome. We believe that this resource will greatly aid researchers in assessing  
751 the impact of newly identified viral variants. Finally, we predicted RBP-binding across 6 other human coronaviruses  
752 (including SARS-CoV-1 and MERS) and identified several conserved binding sites as well newly acquired binding sites  
753 in SARS-CoV-2.

754 All generated results, including fully trained models, predicted binding sites across SARS-CoV-2 and other coron-  
755 aviruses, variant impact scores across 11 viral strains and impact scores of hypothetical variants are publicly available  
756 at <https://sc2rbpmap.helmholtz-muenchen.de/>. We believe that our results give new insight into the role of  
757 RNA-binding proteins in context of SARS-CoV-2 infection and represents a rich resource for further research on how  
758 SARS-CoV-2 hijacks the host cell's RNA regulatory machinery for viral replication and evasion of immune response.

COMPUTATIONAL MAPPING OF THE HUMAN-SARS-COV-2 PROTEIN-RNA INTERACTOME

759 **References**

760 [kno] knowing01.

- 761 [2] Atlante, S., Mongelli, A., Barbi, V., Martelli, F., Farsetti, A., and Gaetano, C. (2020). The epigenetic implication in  
762 coronavirus infection and therapy. *Clinical Epigenetics*, 12(1):156.
- 763 [3] Bartas, M., Brázda, V., Bohálová, N., Cantara, A., Volná, A., Stachurová, T., Malachová, K., Jagelská, E. B.,  
764 Porubiaková, O., Červeň, J., and Pečinka, P. (2020). In-depth bioinformatic analyses of nidovirales including human  
765 sars-cov-2, sars-cov, mers-cov viruses suggest important roles of non-canonical nucleic acid structures in their  
766 lifecycles. *Frontiers in Microbiology*, 11:1583.
- 767 [4] Bojkova, D., Klann, K., Koch, B., Widera, M., Krause, D., Ciesek, S., Cinatl, J., and Münch, C. (2020). Proteomics  
768 of sars-cov-2-infected host cells reveals therapy targets. *Nature*, 583(7816):469–472.
- 769 [5] Budach, S. and Marsico, A. (2018). Pysster: classification of biological sequences by learning sequence and  
770 structure motifs with convolutional neural networks. *Bioinformatics*, 34(17):3035–3037.
- 771 [6] Burgess, H. M., Depledge, D. P., Thompson, L., Srinivas, K. P., Grande, R. C., Vink, E. I., Abebe, J. S., Blackaby,  
772 W. P., Hendrick, A., Albertella, M. R., et al. (2021). Targeting the m6a rna modification pathway blocks sars-cov-2  
773 and hcov-oc43 replication. *Genes & development*, 35(13-14):1005–1019.
- 774 [7] Carithers, L. J., Ardlie, K., Barcus, M., Branton, P. A., Britton, A., Buia, S. A., Compton, C. C., DeLuca, D. S.,  
775 Peter-Demchok, J., Gelfand, E. T., Guan, P., Korzeniewski, G. E., Lockhart, N. C., Rabiner, C. A., Rao, A. K.,  
776 Robinson, K. L., Roche, N. V., Sawyer, S. J., Segrè, A. V., Shive, C. E., Smith, A. M., Sobin, L. H., Undale, A. H.,  
777 Valentino, K. M., Vaught, J., Young, T. R., and Moore, H. M. a. (2015). A novel approach to high-quality postmortem  
778 tissue procurement: The gtx project. *Biopreservation and Biobanking*, 13(5):311–319. PMID: 26484571.
- 779 [8] Caudron-Herger, M., Jansen, R., Wassmer, E., and Diederichs, S. (2021). Rbp2go: a comprehensive pan-species  
780 database on rna-binding proteins, their interactions and functions. *Nucleic Acids Res*, 49(D1):D425–D436.
- 781 [9] Ciccocanti, F., Di Rienzo, M., Romagnoli, A., Colavita, F., Refolo, G., Castilletti, C., Agrati, C., Brai, A., Manetti,  
782 F., Botta, L., Capobianchi, M., Ippolito, G., Piacentini, M., and Fimia, G. (2021). Proteomic analysis identifies the  
783 rna helicase ddx3x as a host target against sars-cov-2 infection. *Antiviral Res*, 190:105064.
- 784 [10] D’Alessandro, A., Thomas, T., Dzieciatkowska, M., Hill, R. C., Francis, R. O., Hudson, K. E., Zimring, J. C., Hod,  
785 E. A., Spitalnik, S. L., and Hansen, K. C. (2020). Serum proteomics in COVID-19 patients: Altered coagulation and  
786 complement status as a function of IL-6 level. *J. Proteome Res.*, 19(11):4417–4427.
- 787 [11] Davey, N. E., Travé, G., and Gibson, T. J. (2011). How viruses hijack cell regulation. *Trends in biochemical  
788 sciences*, 36(3):159–169.
- 789 [12] Demichev, V., Tober-Lau, P., Lemke, O., Nazarenko, T., Thibeault, C., Whitwell, H., Röhl, A., Freiwald, A.,  
790 Szyrwił, L., Ludwig, D., Correia-Melo, C., Aulakh, S. K., Helbig, E. T., Stubbemann, P., Lippert, L. J., Grüning,  
791 N.-M., Blyuss, O., Vernardis, S., White, M., Messner, C. B., Joannidis, M., Sonnweber, T., Klein, S. J., Pizzini,  
792 A., Wohlfarter, Y., Sahanic, S., Hilbe, R., Schaefer, B., Wagner, S., Mittermaier, M., Machleidt, F., Garcia, C.,  
793 Ruwwe-Glösenkamp, C., Lingscheid, T., Bosquillon de Jarcy, L., Stegemann, M. S., Pfeiffer, M., Jürgens, L.,  
794 Denker, S., Zickler, D., Enghard, P., Zeleznik, A., Campbell, A., Hayward, C., Porteous, D. J., Marioni, R. E.,  
795 Uhrig, A., Müller-Redetzky, H., Zoller, H., Löffler-Ragg, J., Keller, M. A., Tancevski, I., Timms, J. F., Zaikin, A.,  
796 Hippenstiel, S., Ramharter, M., Witzentrath, M., Suttorp, N., Lilley, K., Mülleder, M., Sander, L. E., PA-COVID-19  
797 Study group, Ralser, M., and Kurth, F. (2021). A time-resolved proteomic and prognostic map of COVID-19. *Cell  
798 Syst.*, 12(8):780–794.e7.
- 799 [13] Di, B., Jia, H., Luo, O. J., Lin, F., Li, K., Zhang, Y., Wang, H., Liang, H., Fan, J., and Yang, Z. (2020). Identification  
800 and validation of predictive factors for progression to severe COVID-19 pneumonia by proteomics. *Signal Transduct.  
801 Target. Ther.*, 5(1):217.
- 802 [14] Dominguez, D., Freese, P., Alexis, M. S., Su, A., Hochman, M., Palden, T., Bazile, C., Lambert, N. J., Van Nos-  
803 trand, E. L., Pratt, G. A., et al. (2018). Sequence, structure, and context preferences of human rna binding proteins.  
804 *Molecular Cell*, 70(5):854–867.
- 805 [15] Farkas, C., Mella, A., Turgeon, M., and Haigh, J. J. (2021). A novel sars-cov-2 viral sequence bioinformatic  
806 pipeline has found genetic evidence that the viral 3 untranslated region (utr) is evolving and generating increased  
807 viral diversity. *Frontiers in microbiology*, 12.

COMPUTATIONAL MAPPING OF THE HUMAN-SARS-CoV-2 PROTEIN-RNA INTERACTOME

- 808 [16] Feng, H., Bao, S., Rahman, M. A., Weyn-Vanhentenryck, S. M., Khan, A., Wong, J., Shah, A., Flynn, E. D.,  
809 Krainer, A. R., and Zhang, C. (2019). Modeling RNA-Binding Protein Specificity In Vivo by Precisely Registering  
810 Protein-RNA Crosslink Sites. *Molecular Cell*, 74(6):1189–1204.e6.
- 811 [17] Fernandes, J. D., Hinrichs, A. S., Clawson, H., Gonzalez, J. N., Lee, B. T., Nassar, L. R., Raney, B. J., Rosenbloom,  
812 K. R., Nerli, S., Rao, A. A., Schmelter, D., Fyfe, A., Maulding, N., Zweig, A. S., Lowe, T. M., Ares, M., Corbet-  
813 Detig, R., Kent, W. J., Haussler, D., and Haussler, M. (2020). The UCSC SARS-CoV-2 Genome Browser. *Nature*  
814 *Genetics*, 52(10):991–998.
- 815 [18] Flynn, R. A., Belk, J. A., Qi, Y., Yasumoto, Y., Wei, J., Alfajaro, M. M., Shi, Q., Mumbach, M. R., Limaye, A.,  
816 DeWeirdt, P. C., et al. (2021). Discovery and functional interrogation of sars-cov-2 rna-host protein interactions.  
817 *Cell*, 184(9):2394–2411.
- 818 [19] Fu, Y., Jia, G., Pang, X., Wang, R. N., Wang, X., Li, C. J., Smemo, S., Dai, Q., Bailey, K. A., Nobrega, M. A., Han,  
819 K.-L., Cui, Q., and He, C. (2013). FTO-mediated formation of N6-hydroxymethyladenosine and N6-formyladenosine  
820 in mammalian RNA. *Nature Communications*, 4(1).
- 821 [20] Fung, T. S. and Liu, D. X. (2019). Human coronavirus: host-pathogen interaction. *Annual review of microbiology*,  
822 73:529–557.
- 823 [21] Garcia-Moreno, M., Järvelin, A. I., and Castello, A. (2018). Unconventional rna-binding proteins step into the  
824 virus–host battlefield. *Wiley Interdisciplinary Reviews: RNA*, 9(6):e1498.
- 825 [22] Geyer, P. E., Arend, F. M., Doll, S., Louiset, M.-L., Virreira Winter, S., Müller-Reif, J. B., Torun, F. M., Weigand,  
826 M., Eichhorn, P., Bruegel, M., Strauss, M. T., Holdt, L. M., Mann, M., and Teupser, D. (2021). High-resolution  
827 serum proteome trajectories in COVID-19 reveal patient-specific seroconversion. *EMBO Mol. Med.*, 13(8):e14167.
- 828 [23] Ghanbari, M. and Ohler, U. (2020). Deep neural networks for interpreting rna-binding protein target preferences.  
829 *Genome Research*, 30(2):214–226.
- 830 [24] Gordon, D. E., Hiatt, J., Bouhaddou, M., Rezelj, V. V., Ulferts, S., et al. (2020a). Comparative host-coronavirus  
831 protein interaction networks reveal pan-viral disease mechanisms. *Science*, 370(6521):eabe9403.
- 832 [25] Gordon, D. E., Jang, G. M., Bouhaddou, M., Xu, J., Obernier, K., White, K. M., O’Meara, M. J., Rezelj, V. V.,  
833 Guo, J. Z., Swaney, D. L., et al. (2020b). A sars-cov-2 protein interaction map reveals targets for drug repurposing.  
834 *Nature*, 583(7816):459–468.
- 835 [26] Hafner, M., Katsantoni, M., Köster, T., Marks, J., Mukherjee, J., Staiger, D., Ule, J., and Zavolan, M. (2021). Clip  
836 and complementary methods. *Nature Reviews Methods Primers*, 1(1):1–23.
- 837 [27] Haimovich, G., Olender, T., Baez, C., and Gerst, J. E. (2020). Identification and enrichment of secrete cis-acting  
838 rna elements in the coronaviridae and other (+) single-strand rna viruses. *bioRxiv*.
- 839 [28] Hallegger, M., Chakrabarti, A., Lee, F., Lee, B., Amaliotti, A., Odeh, H., Copley, K., Rubien, J., Portz, B., Kuret,  
840 K., Huppertz, I., Rau, F., Patani, R., Fawzi, N., Shorter, J., Luscombe, N., and Ule, J. (2021). Tdp-43 condensation  
841 properties specify its rna-binding and regulatory repertoire. *Cell*, 184(18):637–51.
- 842 [29] Hentze, M. W., Castello, A., Schwarzl, T., and Preiss, T. (2018). A brave new world of rna-binding proteins.  
843 *Nature Reviews Molecular Cell Biology*, 19(5):327–341.
- 844 [30] Hoffmann, H.-H., Sánchez-Rivera, F. J., Schneider, W. M., Luna, J. M., Soto-Feliciano, Y. M., Ashbrook, A. W.,  
845 Le Pen, J., Leal, A. A., Ricardo-Lax, I., Michailidis, E., et al. (2021a). Functional interrogation of a sars-cov-2 host  
846 protein interactome identifies unique and shared coronavirus host factors. *Cell Host & Microbe*, 29(2):267–280.
- 847 [31] Hoffmann, M., Arora, P., Groß, R., Seidel, A., Hörnich, B. F., Hahn, A. S., Krüger, N., Graichen, L., Hofmann-  
848 Winkler, H., Kempf, A., Winkler, M. S., Schulz, S., Jäck, H.-M., Jahrsdörfer, B., Schrezenmeier, H., Müller, M.,  
849 Kleger, A., Münch, J., and Pöhlmann, S. (2021b). SARS-CoV-2 variants B.1.351 and P.1 escape from neutralizing  
850 antibodies. *Cell*, 184(9):2384–2393.e12.
- 851 [32] Hou, Y. J., Chiba, S., Halfmann, P., Ehre, C., Kuroda, M., Dinno III, K. H., Leist, S. R., Schäfer, A., Nakajima,  
852 N., Takahashi, K., et al. (2020). Sars-cov-2 d614g variant exhibits efficient replication ex vivo and transmission in  
853 vivo. *Science*, 370(6523):1464–1468.
- 854 [33] Hu, J., Peng, P., Cao, X., Wu, K., Chen, J., Wang, K., Tang, N., and Huang, A.-I. (2022). Increased immune  
855 escape of the new SARS-CoV-2 variant of concern Omicron. *Cellular and Molecular Immunology*, 19(2):293–295.

COMPUTATIONAL MAPPING OF THE HUMAN-SARS-CoV-2 PROTEIN-RNA INTERACTOME

- 856 [34] Ilias, I., Diamantopoulos, A., Botoula, E., Athanasiou, N., Zacharis, A., Tsipilis, S., Jahaj, E., Vassiliou, A.,  
857 Vassiliadi, D., Kotanidou, A., Tsagarakis, S., and Dimopoulou, I. (2021). Covid-19 and growth hormone/insulin-like  
858 growth factor 1: Study in critically and non-critically ill patients. Front Endocrinol, 12:644055.
- 859 [35] Initiative, C.-. H. G. and Ganna, A. (2021). Mapping the human genetic architecture of covid-19: an update.  
860 medRxiv.
- 861 [36] Jangi, M., Boutz, P., Paul, P., and Sharp, P. (2014). Rbfox2 controls autoregulation in rna-binding protein networks.  
862 Genes Dev, 28(6):637–51.
- 863 [37] Kamel, W., Noerenberg, M., Cerikan, B., Chen, H., Järvelin, A., Kammoun, M., Lee, J., Shuai, N., Garcia-Moreno,  
864 M., Andrejeva, A., Deery, M., Johnson, N., Neufeldt, C., Cortese, M., Knight, M., Lilley, K., Martinez, J., Davis,  
865 I., Bartenschlager, R., Mohammed, S., and Castello, A. (2021). Global analysis of protein-rna interactions in  
866 sars-cov-2-infected cells reveals key regulators of infection. Mol Cell, 81(13):2851–2867.
- 867 [38] Keene, J. (2001). Ribonucleoprotein infrastructure regulating the flow of genetic information between the genome  
868 and the proteome. Proc Natl Acad Sci U S A, 98(19):7018–24.
- 869 [39] Kim, D., Lee, J., Yang, J., Kim, J., Kim, V., and Chang, H. (2020). The architecture of sars-cov-2 transcriptome.  
870 Cell, 181(4):914–921.
- 871 [40] Kim, D.-K., Weller, B., Lin, C.-W., Sheykhkarimli, D., Knapp, J. J., Kishore, N., Sauer, M., Rayhan, A., Young,  
872 V., Marin-de la Rosa, N., Pogoutse, O., et al. (2021). A map of binary sars-cov-2 protein interactions implicates host  
873 immune regulation and ubiquitination. bioRxiv.
- 874 [41] Kingma, D. P. and Ba, J. (2014). Adam: A method for stochastic optimization. arXiv preprint arXiv:1412.6980.
- 875 [42] Kuo, P.-H., Chiang, C.-H., Wang, Y.-T., Doudeva, L. G., and Yuan, H. S. (2014). The crystal structure of  
876 tdp-43 rrm1-dna complex reveals the specific recognition for ug-and tg-rich nucleic acids. Nucleic acids research,  
877 42(7):4712–4722.
- 878 [43] Labeau, A., Lefevre-Utile, A., Bonnet-Madin, L., Fery-Simonian, L., Soumelis, V., Lotteau, V., Vidalain, P.-O.,  
879 Amara, A., and Meertens, L. (2021). Characterization and functional interrogation of sars-cov-2 rna interactome.  
880 BioRxiv.
- 881 [44] Lahaye, X., Gentili, M., Silvin, A., Conrad, C., Picard, L., Jouve, M., Zueva, E., Maurin, M., Nadalin, F., Knott,  
882 G., Zhao, B., Du, F., Rio, M., Amiel, J., Fox, A., Li, P., Etienne, L., Bond, C., Colleaux, L., and Manel, N. (2018).  
883 Nono detects the nuclear hiv capsid to promote cgas-mediated innate immune activation. Cell, 175(2):488–501.
- 884 [45] Lambert, N., Robertson, A., Jangi, M., McGeary, S., Sharp, P., and Burge, C. (2014). Rna bind-n-seq: quantitative  
885 assessment of the sequence and structural binding specificity of rna binding proteins. Molecular Cell, 54(5):887–900.
- 886 [46] Lee, S., Lee, Y.-s., Choi, Y., Son, A., Park, Y., Lee, K.-M., Kim, J., Kim, J.-S., and Kim, V. N. (2021). The  
887 sars-cov-2 rna interactome. Molecular Cell.
- 888 [47] Li, Z. and Nagy, P. (2011a). Diverse roles of host rna binding proteins in rna virus replication. RNA Biol,  
889 8(2):305–15.
- 890 [48] Li, Z. and Nagy, P. D. (2011b). Diverse roles of host rna binding proteins in rna virus replication. RNA biology,  
891 8(2):305–315.
- 892 [49] Licata, L., Lo Surdo, P., Iannuccelli, M., Palma, A., Micarelli, E., Perfetto, L., Peluso, D., Calderone, A.,  
893 Castagnoli, L., and Cesareni, G. (2020). Signor 2.0, the signaling network open resource 2.0: 2019 update. Nucleic  
894 Acids Res, 48(D1):D504–D510.
- 895 [50] Liu, H., Wei, P., Kappler, J. W., Marrack, P., and Zhang, G. (2022). SARS-CoV-2 Variants of Concern and Variants  
896 of Interest Receptor Binding Domain Mutations and Virus Infectivity. Frontiers in Immunology, 13:825256.
- 897 [51] Liu, J., Xu, Y.-P., Li, K., Ye, Q., Zhou, H.-Y., Sun, H., Li, X., Yu, L., Deng, Y.-Q., Li, R.-T., Cheng, M.-L., He, B.,  
898 Zhou, J., Li, X.-F., Wu, A., Yi, C., and Qin, C.-F. (2021a). The m6A methylome of SARS-CoV-2 in host cells. Cell  
899 Research, 31(4).
- 900 [52] Liu, Y., Liu, J., Johnson, B. A., Xia, H., Ku, Z., Schindewolf, C., Widen, S. G., An, Z., Weaver, S. C., Menachery,  
901 V. D., Xie, X., and Shi, P.-Y. (2021b). Delta spike P681R mutation enhances SARS-CoV-2 fitness over Alpha variant.  
902 bioRxiv, page 2021.08.12.456173.

COMPUTATIONAL MAPPING OF THE HUMAN-SARS-CoV-2 PROTEIN-RNA INTERACTOME

- 903 [53] Lubinski, B., Frazier, L. E., Phan, M. V. T., Bugembe, D. L., Tang, T., Daniel, S., Cotten, M., Jaimes, J. A.,  
904 and Whittaker, G. R. (2021). Spike protein cleavage-activation mediated by the SARS-CoV-2 P681R mutation: a  
905 case-study from its first appearance in variant of interest (VOI) A.23.1 identified in Uganda. Technical report.
- 906 [54] Luo, H., Chen, Q., Chen, J., Chen, K., Shen, X., and Jiang, H. (2005). The nucleocapsid protein of sars  
907 coronavirus has a high binding affinity to the human cellular heterogeneous nuclear ribonucleoprotein a1. FEBS  
908 letters, 579(12):2623–2628.
- 909 [55] Mahiet, C. and Swanson, C. M. (2016). Control of HIV-1 gene expression by SR proteins. Biochemical Society  
910 Transactions, 44(5):1417–1425.
- 911 [56] Manokaran, G., Finol, E., Wang, C., Gunaratne, J., Bahl, J., Ong, E., Tan, H., Sessions, O., Ward, A., Gubler,  
912 D., Harris, E., Garcia-Blanco, M., and Ooi, E. (2015). Dengue subgenomic rna binds trim25 to inhibit interferon  
913 expression for epidemiological fitness. Science, 9(350):6257.
- 914 [57] Messner, C. B., Demichev, V., Wendisch, D., Michalick, L., White, M., Freiwald, A., Textoris-Taube, K.,  
915 Vernardis, S. I., Egger, A.-S., Kreidl, M., Ludwig, D., Kilian, C., Agostini, F., Zelezniak, A., Thibeault, C., Pfeiffer,  
916 M., Hippenstiel, S., Hocke, A., von Kalle, C., Campbell, A., Hayward, C., Porteous, D. J., Marioni, R. E., Langenberg,  
917 C., Lilley, K. S., Kuebler, W. M., Mülleider, M., Drosten, C., Suttorp, N., Witzenth, M., Kurth, F., Sander, L. E.,  
918 and Ralsler, M. (2020). Ultra-high-throughput clinical proteomics reveals classifiers of COVID-19 infection. Cell  
919 Syst., 11(1):11–24.e4.
- 920 [58] Meyer, K. D., Saletore, Y., Zumbo, P., Elemento, O., Mason, C. E., and Jaffrey, S. R. (2012). Comprehensive  
921 analysis of mrna methylation reveals enrichment in 3 utrs and near stop codons. Cell, 149(7):1635–1646.
- 922 [59] Molleston, J. M. and Cherry, S. (2017). Attacked from all sides: Rna decay in antiviral defense. Viruses, 9(1):2.
- 923 [60] Mukherjee, M. and Goswami, S. (2020). Global cataloguing of variations in untranslated regions of viral genome  
924 and prediction of key host rna binding protein-microrna interactions modulating genome stability in sars-cov-2. PLoS  
925 one, 15(8):e0237559.
- 926 [61] Mukherjee, N., Wessels, H., Lebedeva, S., Sajek, M., Ghanbari, M., Garzia, A., Munteanu, A., Yusuf, D., Farazi,  
927 T., Hoell, J., Akat, K., Akalin, A., Tuschl, and Ohler, U. (2019). Deciphering human ribonucleoprotein regulatory  
928 networks. Nucleic Acids Res, 47(2):570–581.
- 929 [62] Nabeel-Shah, S., Lee, H., Ahmed, N., Burke, G., Farhangmehr, S., Ashraf, K., Pu, S., Braunschweig, U., Zhong,  
930 G., Wei, H., Tang, H., Yang, J., Marcon, E., Blencowe, B., Zhang, Z., and Greenblatt, J. (2022). Sars-cov-2  
931 nucleocapsid protein binds host mRNAs and attenuates stress granules to impair host stress response. iScience,  
932 25(1):103562.
- 933 [63] Overmyer, K., Shishkova, E., Miller, I., Balnis, J., Bernstein, M., Peters-Clarke, T., Meyer, J., Quan, Q.,  
934 Muehlbauer, L., Trujillo, E., and He, Y. e. a. (2021). Large-scale multi-omic analysis of covid-19 severity. Cell Syst,  
935 12(1):23–40.
- 936 [64] Pairo-Castineira, E., Clohisey, S., Klaric, L., Bretherick, A. D., Rawlik, K., Pasko, D., Walker, S., Parkinson, N.,  
937 Fourman, M. H., Russell, C. D., Furniss, J., Richmond, A., Gountouna, E., Wrobel, N., Harrison, D., Wang, B.,  
938 Wu, Y., Meynert, A., Griffiths, F., Oosthuyzen, W., Kousathanas, A., Moutsianas, L., Yang, Z., Zhai, R., Zheng,  
939 C., Grimes, G., Beale, R., Millar, J., Shih, B., Keating, S., Zechner, M., Haley, C., Porteous, D. J., Hayward, C.,  
940 Yang, J., Knight, J., Summers, C., Shankar-Hari, M., Klenerman, P., Turtle, L., Ho, A., Moore, S. C., Hinds, C.,  
941 Horby, P., Nichol, A., Maslove, D., Ling, L., McAuley, D., Montgomery, H., Walsh, T., Pereira, A. C., Renieri, A.,  
942 GenOMICC Investigators, ISARIC4C Investigators, COVID-19 Human Genetics Initiative, 23andMe Investigators,  
943 BRACOVIC Investigators, Gen-COVID Investigators, Shen, X., Ponting, C. P., Fawkes, A., Tenesa, A., Caulfield,  
944 M., Scott, R., Rowan, K., Murphy, L., Openshaw, P. J. M., Semple, M. G., Law, A., Vitart, V., Wilson, J. F., and  
945 Baillie, J. K. (2021). Genetic mechanisms of critical illness in COVID-19. Nature, 591(7848):92–98.
- 946 [65] Pennemann, F., Mussabekova, A., Urban, C., Stukalov, A., Andersen, L., Grass, V., Lavacca, T., Holze, C.,  
947 Oubraham, L., Benamrouche, Y., Girardi, E., Boulos, R., Hartmann, R., Superti-Furga, G., Habjan, M., Imler, J.,  
948 Meignin, C., and Pichlmair, A. (2021). Cross-species analysis of viral nucleic acid interacting proteins identifies  
949 taoks as innate immune regulators. Nat Commun, 12(1):7009.
- 950 [66] Rothamel, K., Arcos, S., Kim, B., Reasoner, C., Lisy, S., Mukherjee, N., and Ascano, M. (2021). Elavl1 primarily  
951 couples mrna stability with the 3' utrs of interferon-stimulated genes. Cell Rep, 35(8):109178.

COMPUTATIONAL MAPPING OF THE HUMAN-SARS-CoV-2 PROTEIN-RNA INTERACTOME

- 952 [67] Sanyaolu, A., Okorie, C., Marinkovic, A., Haider, N., Abbasi, A. F., Jafari, U., Prakash, S., and Balendra, V. (2021).  
953 The emerging sars-cov-2 variants of concern. Therapeutic advances in infectious disease, 8:20499361211024372.
- 954 [68] Sayers, E. W., Beck, J., Bolton, E. E., Bourexis, D., Brister, J. R., Canese, K., Comeau, D. C., Funk, K., Kim, S.,  
955 Klimke, W., et al. (2021). Database resources of the national center for biotechnology information. Nucleic acids  
956 research, 49(D1):D10.
- 957 [69] Schmidt, N., Lareau, C. A., Keshishian, H., Ganskih, S., Schneider, C., Hennig, T., Melanson, R., Werner, S., Wei,  
958 Y., Zimmer, M., et al. (2021). The sars-cov-2 rna-protein interactome in infected human cells. Nature Microbiology,  
959 6(3):339–353.
- 960 [70] Schneider, W. M., Luna, J. M., Hoffmann, H.-H., Sánchez-Rivera, F. J., Leal, A. A., Ashbrook, A. W., Le Pen,  
961 J., Ricardo-Lax, I., Michailidis, E., Peace, A., Stenzel, A. F., Lowe, S. W., MacDonald, M. R., Rice, C. M., and  
962 Poirier, J. T. (2021). Genome-scale identification of sars-cov-2 and pan-coronavirus host factor networks. Cell,  
963 184(1):120–132.e14.
- 964 [71] Shen, B., Yi, X., Sun, Y., Bi, X., Du, J., Zhang, C., Quan, S., Zhang, F., Sun, R., Qian, L., Ge, W., Liu, W., Liang,  
965 S., Chen, H., Zhang, Y., Li, J., Xu, J., He, Z., Chen, B., Wang, J., Yan, H., Zheng, Y., Wang, D., Zhu, J., Kong, Z.,  
966 Kang, Z., Liang, X., Ding, X., Ruan, G., Xiang, N., Cai, X., Gao, H., Li, L., Li, S., Xiao, Q., Lu, T., Zhu, Y., Liu,  
967 H., Chen, H., and Guo, T. (2020). Proteomic and metabolomic characterization of COVID-19 patient sera. Cell,  
968 182(1):59–72.e15.
- 969 [72] Sievers, F. and Higgins, D. G. (2014). Clustal omega, accurate alignment of very large numbers of sequences. In  
970 Multiple sequence alignment methods, pages 105–116. Springer.
- 971 [73] Sola, I., Almazán, F., Zúñiga, S., and Enjuanes, L. (2015). Continuous and discontinuous rna synthesis in  
972 coronaviruses. Annu Rev Virol, 1(3):265–88.
- 973 [74] Soto-Acosta, R., Xie, X., Shan, C., Baker, C. K., Shi, P.-Y., Rossi, S. L., Garcia-Blanco, M. A., and Bradrick,  
974 S. (2018). Fragile x mental retardation protein is a zika virus restriction factor that is antagonized by subgenomic  
975 flaviviral rna. Elife, 7:e39023.
- 976 [75] Srivastava, N., Hinton, G., Krizhevsky, A., Sutskever, I., and Salakhutdinov, R. (2014). Dropout: a simple way to  
977 prevent neural networks from overfitting. The journal of machine learning research, 15(1):1929–1958.
- 978 [76] Srivastava, R., Daulatabad, S. V., Srivastava, M., and Janga, S. C. (2020). Role of SARS-CoV-2 in altering  
979 the RNA binding protein and miRNA directed post-transcriptional regulatory networks in humans. bioRxiv, page  
980 2020.07.06.190348.
- 981 [77] Stelzer, G., Rosen, N., Plaschkes, I., Zimmermann, S., Twik, M., Fishilevich, S., Stein, T. I., Nudel, R., Lieder, I.,  
982 Mazor, Y., et al. (2016). The genecards suite: from gene data mining to disease genome sequence analyses. Current  
983 protocols in bioinformatics, 54(1):1–30.
- 984 [78] Stukalov, A., Girault, V., Grass, V., Karayel, O., Bergant, V., Urban, C., Haas, D. A., Huang, Y., Oubraham, L.,  
985 Wang, A., Hamad, M. S., et al. (2021). Multilevel proteomics reveals host perturbations by sars-cov-2 and sars-cov.  
986 Nature, 594(7862):246–252.
- 987 [79] Sugimoto, Y., König, J., Hussain, S., Zupan, B., Curk, T., Frye, M., and Ule, J. (2012). Analysis of clip and iclip  
988 methods for nucleotide-resolution studies of protein-rna interactions. Genome biology, 13(8):1–13.
- 989 [80] Sun, L., Li, P., Ju, X., Rao, J., Huang, W., Ren, L., Zhang, S., Xiong, T., Xu, K., Zhou, X., Gong, M., Miska,  
990 E., Ding, Q., Wang, J., and Zhang, Q. C. (2021). In vivo structural characterization of the sars-cov-2 rna genome  
991 identifies host proteins vulnerable to repurposed drugs. Cell, 184(7):1865–1883.e20.
- 992 [81] Sundararajan, M., Taly, A., and Yan, Q. (2017). Axiomatic attribution for deep networks. In International  
993 Conference on Machine Learning, pages 3319–3328. PMLR.
- 994 [82] Teplova, M., Hafner, M., Teplov, D., Essig, K., Tuschl, T., and Patel, D. (2013). Structure-function studies of star  
995 family quaking proteins bound to their in vivo rna target sites. Genes Dev, 27(8):928–40.
- 996 [83] Tirumuru, N., Zhao, B., Lu, W., Lu, Z., C, H., and Wu, L. (2016). N(6)-methyladenosine of hiv-1 rna regulates  
997 viral infection and hiv-1 gag protein expression. Elife, 5:e15528.
- 998 [84] Ulrich, L., Halwe, N. J., Taddeo, A., Ebert, N., Schön, J., Devisme, C., Trüeb, B. S., Hoffmann, B., Wider, M., Fan,  
999 X., et al. (2022). Enhanced fitness of sars-cov-2 variant of concern alpha but not beta. Nature, 602(7896):307–313.

COMPUTATIONAL MAPPING OF THE HUMAN-SARS-COV-2 PROTEIN-RNA INTERACTOME

- 1000 [85] Van Nostrand, E., Freese, P., Pratt, G., Wang, X., Wei, X., Xiao, R., Blue, S., Chen, J., Cody, N., and Dominguez,  
1001 D. (2020a). A large-scale binding and functional map of human rna-binding proteins. Nature, 583(7818):711–719.
- 1002 [86] Van Nostrand, E. L., Freese, P., Pratt, G. A., Wang, X., Wei, X., Xiao, R., Blue, S. M., Chen, J.-Y., Cody, N. A.,  
1003 Dominguez, D., et al. (2020b). A large-scale binding and functional map of human rna-binding proteins. Nature,  
1004 583(7818):711–719.
- 1005 [87] Vandelli, A., Monti, M., Milanetti, E., Armaos, A., Rupert, J., Zacco, E., Bechara, E., Delli Ponti, R., and Tartaglia,  
1006 G. G. (2020). Structural analysis of sars-cov-2 genome and predictions of the human interactome. Nucleic Acids  
1007 Research, 48(20):11270–11283.
- 1008 [88] Vashist, S., Urena, L., Chaudhry, Y., and Goodfellow, I. (2012). Identification of rna-protein interaction networks  
1009 involved in the norovirus life cycle. J Virol, 86(22):11977–90.
- 1010 [89] Verma, R., Saha, S., Kumar, S., Mani, S., Maiti, T. K., and Surjit, M. (2021). RNA-protein interaction analysis of  
1011 SARS-CoV-2 5' and 3' untranslated regions reveals a role of lysosome-associated membrane protein-2a during viral  
1012 infection. mSystems, 6(4):e0064321.
- 1013 [90] V'kovski, P., Kratzel, A., Steiner, S., Stalder, H., and Thiel, V. (2021). Coronavirus biology and replication:  
1014 implications for sars-cov-2. Nature Reviews Microbiology, 19(3):155–170.
- 1015 [91] Wang, R., Simoneau, C. R., Kulsuptrakul, J., Bouhaddou, M., Travisano, K. A., Hayashi, J. M., Carlson-Stevermer,  
1016 J., Zengel, J. R., Richards, C. M., Fozouni, P., Oki, J., Rodriguez, L., Joehnk, B., Walcott, K., Holden, K., Sil,  
1017 A., Carette, J. E., Krogan, N. J., Ott, M., and Puschnik, A. S. (2021). Genetic screens identify host factors for  
1018 SARS-CoV-2 and common cold coronaviruses. Cell, 184(1):106–119.e14.
- 1019 [92] Wei, J., Alfajaro, M. M., DeWeirdt, P. C., Hanna, R. E., Lu-Culligan, W. J., Cai, W. L., Strine, M. S., Zhang,  
1020 S.-M., Graziano, V. R., Schmitz, C. O., et al. (2021). Genome-wide crispr screens reveal host factors critical for  
1021 sars-cov-2 infection. Cell, 184(1):76–91.e13.
- 1022 [93] Wheeler, E. C., Van Nostrand, E. L., and Yeo, G. W. (2018). Advances and challenges in the detection of  
1023 transcriptome-wide protein–rna interactions. Wiley Interdisciplinary Reviews: RNA, 9(1):e1436.
- 1024 [94] Wu, C.-H., Chen, P.-J., and Yeh, S.-H. (2014). Nucleocapsid phosphorylation and rna helicase ddx1 recruitment  
1025 enables coronavirus transition from discontinuous to continuous transcription. Cell host & microbe, 16(4):462–472.
- 1026 [95] Wu, P., Chen, D., Ding, W., Wu, P., Hou, H., Bai, Y., Zhou, Y., Li, K., Xiang, S., Liu, P., Ju, J., Guo, E., Liu, J.,  
1027 Yang, B., Fan, J., He, L., Sun, Z., Feng, L., Wang, J., Wu, T., Wang, H., Cheng, J., Xing, H., Meng, Y., Li, Y., Zhang,  
1028 Y., Luo, H., Xie, G., Lan, X., Tao, Y., Li, J., Yuan, H., Huang, K., Sun, W., Qian, X., Li, Z., Huang, M., Ding, P.,  
1029 Wang, H., Qiu, J., Wang, F., Wang, S., Zhu, J., Ding, X., Chai, C., Liang, L., Wang, X., Luo, L., Sun, Y., Yang, Y.,  
1030 Zhuang, Z., Li, T., Tian, L., Zhang, S., Zhu, L., Chang, A., Chen, L., Wu, Y., Ma, X., Chen, F., Ren, Y., Xu, X.,  
1031 Liu, S., Wang, J., Yang, H., Wang, L., Sun, C., Ma, D., Jin, X., and Chen, G. (2021). The trans-omics landscape of  
1032 COVID-19. Nat. Commun., 12(1):4543.
- 1033 [96] Xiang, J. S., Mueller, J. R., Luo, E.-C., Yee, B., Schafer, D., Schmok, J. C., Tan, F. E., Her, H.-L., Chen, C.-Y.,  
1034 Brannan, K. W., Jones, K. L., Park, S. S., Jin, W., McVicar, R., Kwong, E. M., Le, P., Kofman, E., Vu, A. Q., Li,  
1035 Y., Tankka, A. T., Dong, K. D., Song, Y., Carlin, A. F., Van Nostrand, E. L., Leibel, S. L., and Yeo, G. W. (2021).  
1036 Discovery and Functional Interrogation of the Virus and Host RNA Interactome of SARS-Cov-2 Proteins. SSRN  
1037 Scholarly Paper 3867726, Social Science Research Network, Rochester, NY.
- 1038 [97] Zannella, C., Rinaldi, L., Boccia, G., Chianese, A., Sasso, F. C., De Caro, F., Franci, G., and Galdiero, M. (2021).  
1039 Regulation of m6a methylation as a new therapeutic option against covid-19. Pharmaceuticals, 14(11):1135.
- 1040 [98] Zhang, J., Xiao, T., Cai, Y., Lavine, C. L., Peng, H., Zhu, H., Anand, K., Tong, P., Gautam, A., Mayer, M. L.,  
1041 Walsh, R. M., Rits-Volloch, S., Wesemann, D. R., Yang, W., Seaman, M. S., Lu, J., and Chen, B. (2021). Membrane  
1042 fusion and immune evasion by the spike protein of SARS-CoV-2 Delta variant. Technical report.
- 1043 [99] Zhang, X., Hao, H., Ma, L., Zhang, Y., Hu, X., Chen, Z., Liu, D., Yuan, J., Hu, Z., and Guan, W. (2020).  
1044 Methyltransferase-like 3 modulates severe acute respiratory syndrome coronavirus-2 rna n6-methyladenosine  
1045 modification and replication. bioRxiv.



## COMPUTATIONAL MAPPING OF THE HUMAN-SARS-CoV-2 PROTEIN-RNA INTERACTOME

### 1046 **Code and Data Availability**

1047 Training data and pre-trained models, together with scripts for training and prediction are available at <https://github.com/mhorlacher/sc2rbpmap>. RBP binding sites on the SARS-CoV-2 genome and variant impact scores for 11 viral  
1048 strains are available at <https://sc2rbpmap.helmholtz-munich.de>.  
1049

## COMPUTATIONAL MAPPING OF THE HUMAN-SARS-CoV-2 PROTEIN-RNA INTERACTOME

### 1050 **Acknowledgments**

1051 This work was supported by the Helmholtz Association under the joint research school "Munich School for Data  
1052 Science - MUDS to M.H., S.O., G.C., P.S. and A.M., the Deutsche Forschungsgemeinschaft (SFB/TR501 84 TP C01)  
1053 to A.M. and L.M., the Helmholtz Association AeroHEALTH grant to A.M. and Y.H., additionally supported by the  
1054 Joachim Herz Foundation for Y.H. MG and UO are supported by the Berlin Center of Machine Learning (BZML)  
1055 funded by the German Ministry for Education and Research (BMBF).

## COMPUTATIONAL MAPPING OF THE HUMAN-SARS-CoV-2 PROTEIN-RNA INTERACTOME

### 1056 **Author Contributions**

1057 **Marc Horlacher:** Conceptualization; Data pre-processing and curation; Machine learning model training and pre-  
1058 diction; comparative genomics analysis; viral strains analysis; Interpretation of results; Visualisation; Methodology;  
1059 Implementation of the Dashboard; Writing – original draft; Writing – review & editing. **Svitlana Oleshko:** Conceptual-  
1060 ization; Data curation; RBP map clustering and visualisation; SECRete motif and viral strains analysis; Interpretation  
1061 of results; Writing – review & editing. **Yue Hu:** Conceptualization; Data curation; model predictions; downstream  
1062 statistical analysis; viral strains analysis; Interpretation of results; Methodology; Writing – review & editing. **Mahsa**  
1063 **Ghanbari:** Analysis of PARCLIP data and machine learning model training; Writing – review & editing. **Giulia**  
1064 **Cantini:** Implementation of the Dashboard. **Patrick Schinke:** Implementation of the Dashboard. **Ernesto Elorduy**  
1065 **Vergara:** Conceptualization; Methodology. **Florian Bittner:** Software engineering for public data integration and  
1066 analysis. **Nikola S. Mueller:** Conceptualization; Supervision; Public data curation and analysis; Visualisation; Writing  
1067 – original draft; Writing – review & editing. **Uwe Ohler:** Conceptualization; Supervision; Funding acquisition and  
1068 resources. **Lamber Moyon:** Conceptualization; Supervision; Viral strain analysis; Interpretation of the results; Visuali-  
1069 sation; Methodology; Writing – original draft; Writing – review & editing. **Annalisa Marsico:** Conceptualization;  
1070 Supervision; Methodology; Visualisation; Interpretation of the results; Funding acquisition and resources; Writing –  
1071 original draft; Writing – review & editing.

COMPUTATIONAL MAPPING OF THE HUMAN-SARS-COV-2 PROTEIN-RNA INTERACTOME

1072 **Conflict of Interest Statement**

1073 Authors F.B. and N.S.M. hold positions at knowing01 GmbH that might benefit or be at a disadvantage from the  
1074 published findings. The remaining authors declare no conflict of interest that is relevant to the content of this article.

COMPUTATIONAL MAPPING OF THE HUMAN-SARS-CoV-2 PROTEIN-RNA INTERACTOME

1075 **6 Tables**

Table 1: Subset of high delta score mutations passing binding sites thresholds

	RBP	Variant	Strain	Genomic element	REF score	ALT score	delta score	Impact
0	SRSF7	G210T	delta, kappa	5' UTR	0.768	0.457	-0.311	loss
1	RBM20	C3267T	alpha	ORF1ab	0.813	0.336	-0.477	loss
2	RBM22	C18877T	mu	ORF1ab	0.338	0.614	0.276	gain
3	HNRNPC	C21575T	iota	S	0.374	0.840	0.467	gain
4	MBNL1	del_22281	beta	S	0.800	0.006	-0.795	loss
5	ELAVL1	del_22299	lambda	S	0.070	0.632	0.562	gain
6	SF3B4	del_22299	lambda	S	0.871	0.128	-0.744	loss
7	SF3A3	del_22299	lambda	S	0.860	0.273	-0.587	loss
8	U2AF2	del_22299	lambda	S	0.543	0.980	0.438	gain
9	GPKOW	del_22299	lambda	S	0.297	0.841	0.544	gain
10	MBNL1	del_22299	lambda	S	0.803	0.398	-0.405	loss
11	SF3A3	C22995A	omicron	S	0.081	0.808	0.726	gain
12	ORF1	A23013C	omicron	S	0.014	0.621	0.608	gain
13	ORF1	A23040G	omicron	S	0.006	0.673	0.666	gain
14	ORF1	G23048A	omicron	S	0.006	0.606	0.600	gain
15	SND1	G23048A	omicron	S	0.187	0.791	0.604	gain
16	SRSF7	C23604A	alpha, mu	S	0.394	0.719	0.326	gain
17	SRSF7	C23604G	delta, kappa	S	0.394	0.792	0.398	gain
18	HNRNPC	C25469T	delta, kappa	ORF3a	0.317	0.670	0.352	gain
19	FTO	G25563T	beta, epsilon, iota, mu	ORF3a	0.633	0.080	-0.552	loss
20	FTO	del_28278	eta	N	0.335	0.683	0.348	gain
21	FTO	G28280C	alpha	N	0.679	0.209	-0.470	loss
22	ORF1	A28699G	eta	N	0.597	0.141	-0.456	loss

## COMPUTATIONAL MAPPING OF THE HUMAN-SARS-COV-2 PROTEIN-RNA INTERACTOME

### 1076 **7 Figures**

COMPUTATIONAL MAPPING OF THE HUMAN-SARS-CoV-2 PROTEIN-RNA INTERACTOME

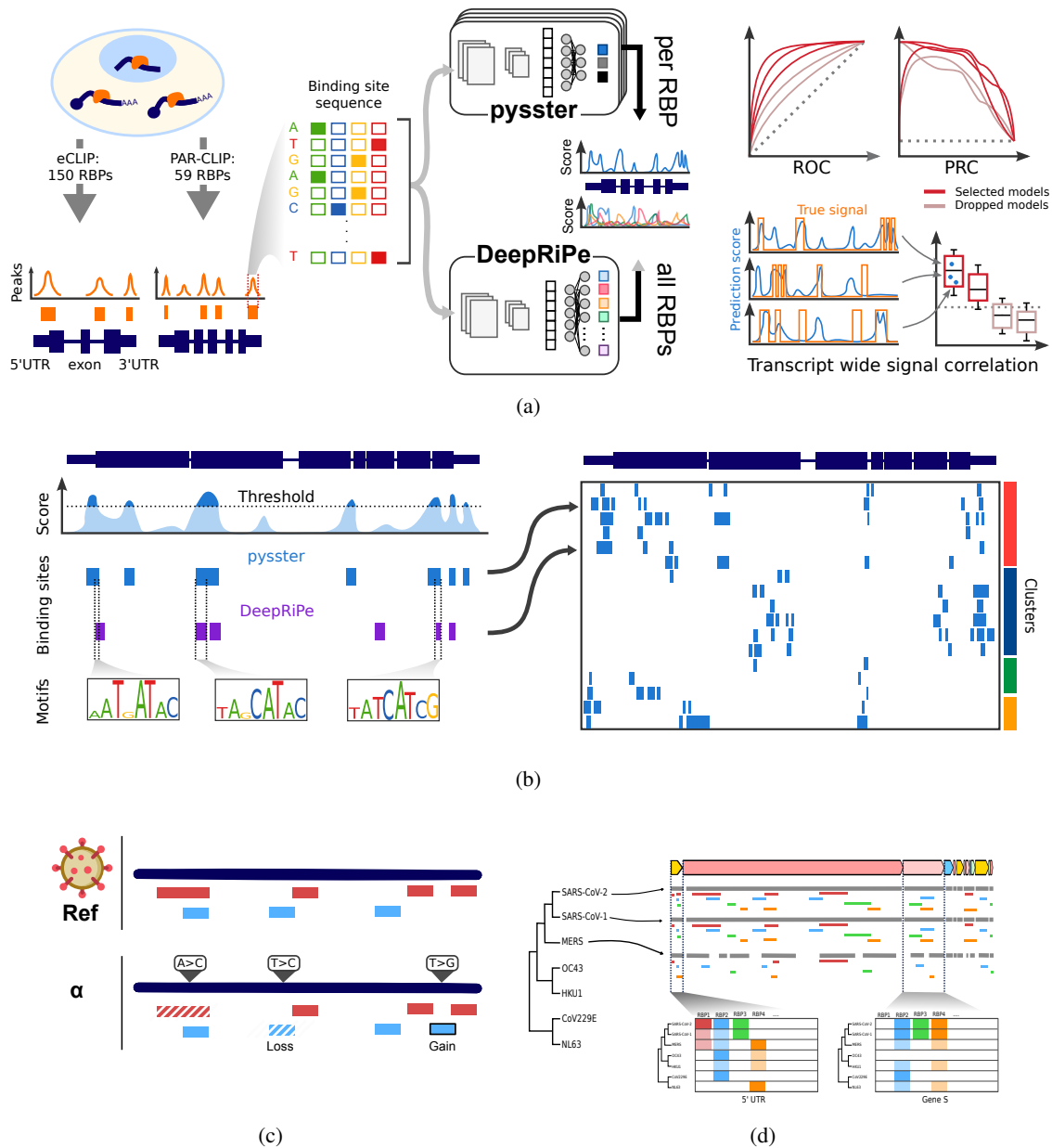
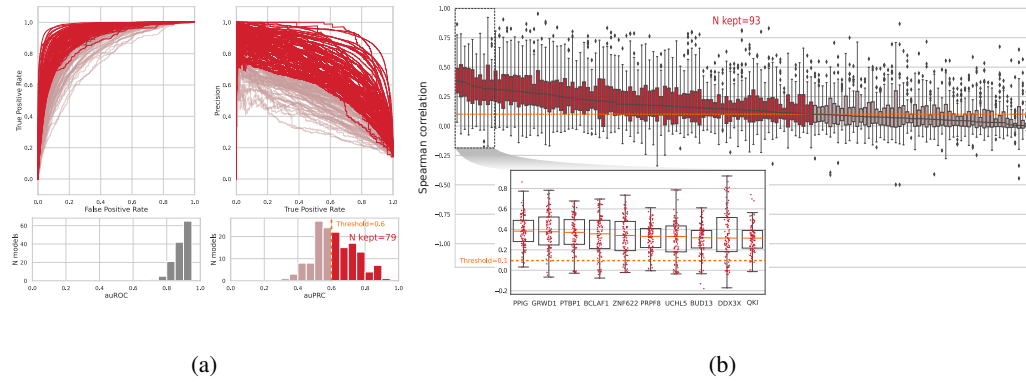


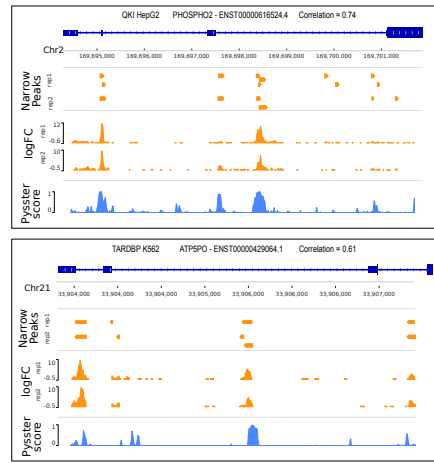
Figure 1: Pipeline of the computational mapping of the human - SARS-CoV-2 protein-RNA interactome. **a.** (Left panel) Interactions between RNA-binding proteins (RBPs) and transcripts can be experimentally measured through eCLIP and PAR-CLIP protocols, enabling the quantification of locally accumulated reads, and the calling of peaks. Such peaks were obtained for 150 RBPs from eCLIP data (86), and for 59 RBPs from PAR-CLIP data (61). (Middle panel) Sequences from these peaks were used to train two deep learning models, composed of convolutional neural networks enabling the detection of complex sequence motifs. These models can then be applied to predict for a given sequence its potential for binding by a RBP. The *pysster* models are trained separately for each RBP, while *DeepRiPe* is trained in a multi-task fashion and simultaneously for all input RBPs. (Right panel) A selection of high-performance models was established through evaluation of performance of the models, from overall performance metrics to in-practice, sequence-wide evaluation. **b.** All retained models were applied to scan the entire genome of SARS-CoV-2, and binding sites were predicted from consecutive, high-prediction scores positions. Sequence motifs underlying RBP binding sites were also identified by interrogating both CNNs via Integrated Gradients. Predictions were compiled in the first *in silico* map of host-protein - viral RNA interactome for SARS-CoV-2. **c** The prediction models were applied to evaluate the impact of variants of concerns, **d** as well as to evaluate the evolutionary trajectory of affinity of host RBPs to other coronaviruses' genomes.

COMPUTATIONAL MAPPING OF THE HUMAN-SARS-CoV-2 PROTEIN-RNA INTERACTOME

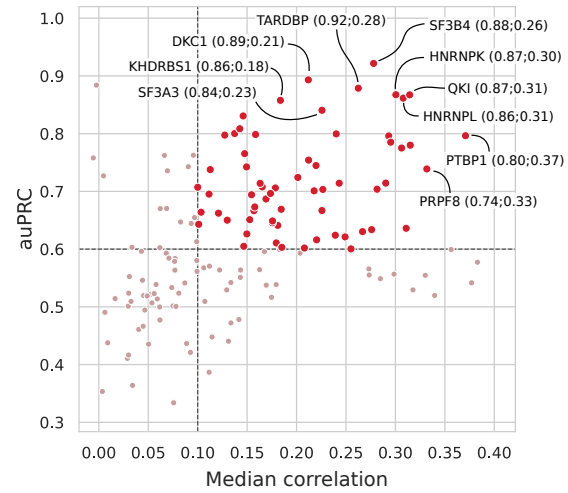


(a)

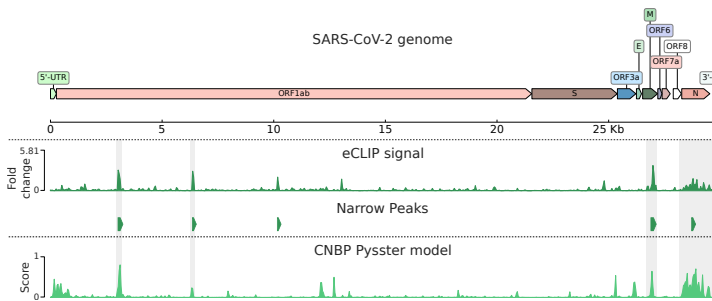
(b)



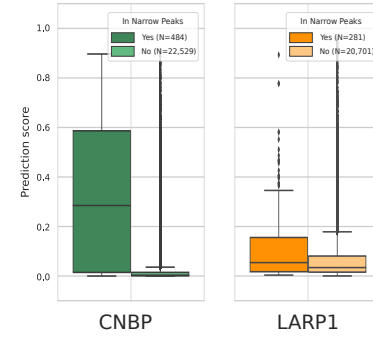
(c)



(d)



(e)



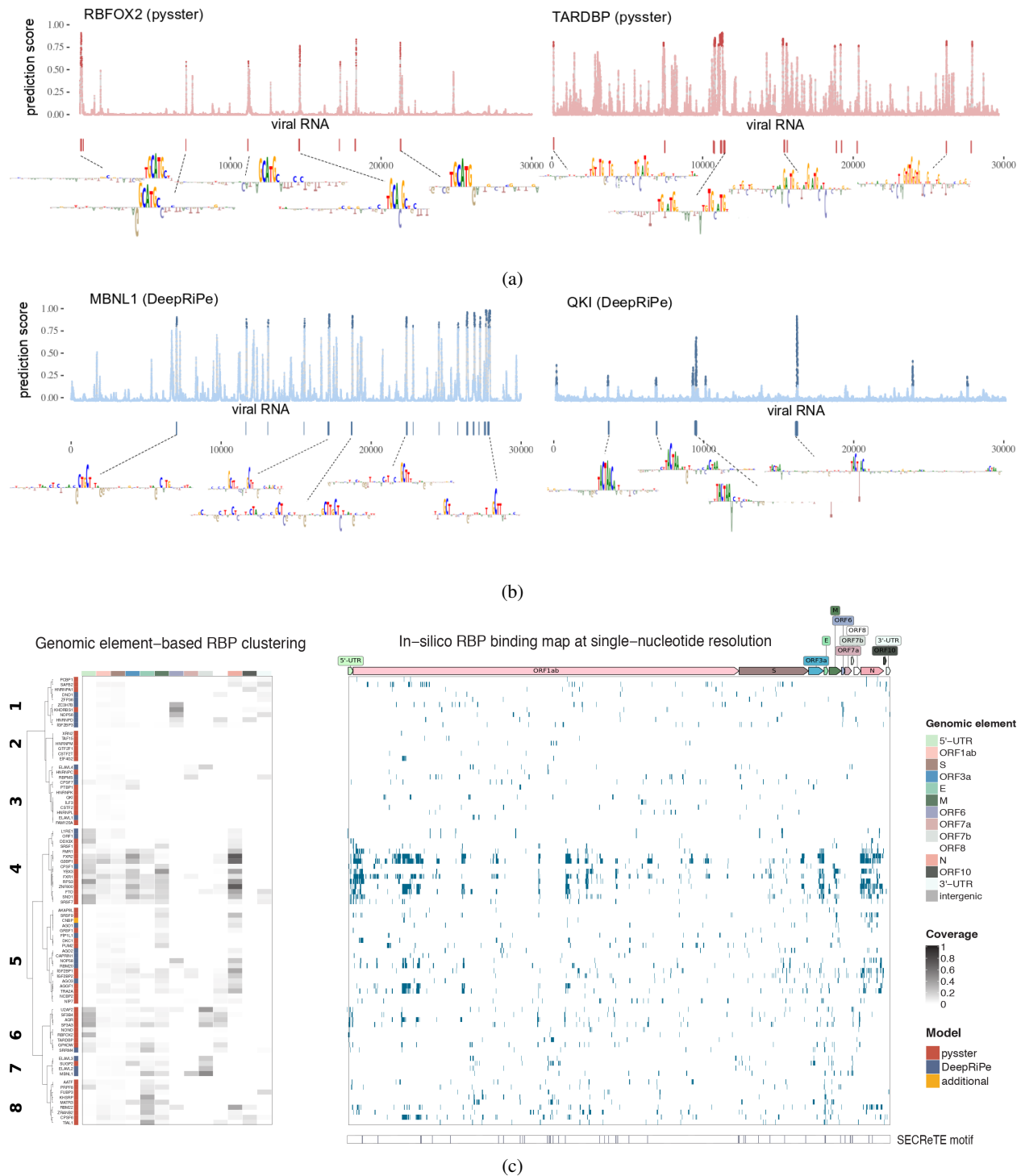
(f)



## COMPUTATIONAL MAPPING OF THE HUMAN-SARS-CoV-2 PROTEIN-RNA INTERACTOME

Figure 2: Evaluation of pysster models' performance and high-quality model selection. **a.** Receiver Operating Curve (ROC) and Precision Recall Curve (PRC) for all 150 pysster models trained from ENCODE eCLIP datasets. A first threshold of 0.6 was set on the area under the PRCs (auPRC), leading to a subset of 79 models passing the threshold. **b.** Boxplots of correlations between eCLIP and prediction scores from 100 left-out transcripts per RBP model. This correlation highlights the performance of models in a realistic context of full-sequence-length scan. A second threshold was thus set on the median correlation coefficient, leading to a subset of 93 models passing the threshold. The 10 models with highest median correlation are displayed in a detailed sub-plot. **c.** Genome-browser view illustrating the comparison between eCLIP signals and model prediction scores over full-length transcripts. Two of the best models are presented, with signal from left-out transcripts with high correlation between eCLIP log-fold-change signals and prediction scores from the pysster models. **d.** Scatterplot of the AUPRC and median correlation values for each model, highlighting the final subset of high-quality models. The top 10 models are labeled. **e.** Comparison of genome-wide eCLIP signal and pysster prediction scores from the CNBP eCLIP datasets generated over the SARS-CoV-2 genome by (69). **f.** Boxplot of pysster prediction scores from position within or without overlap from called narrow peaks, for the CNBP model and the LARP1 model.

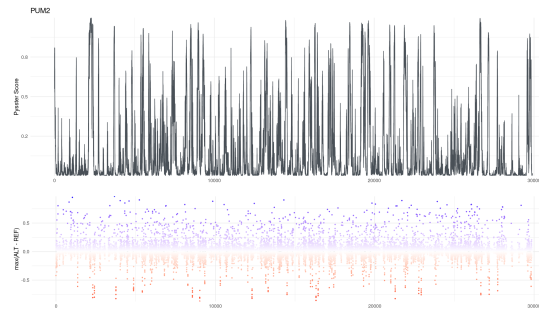
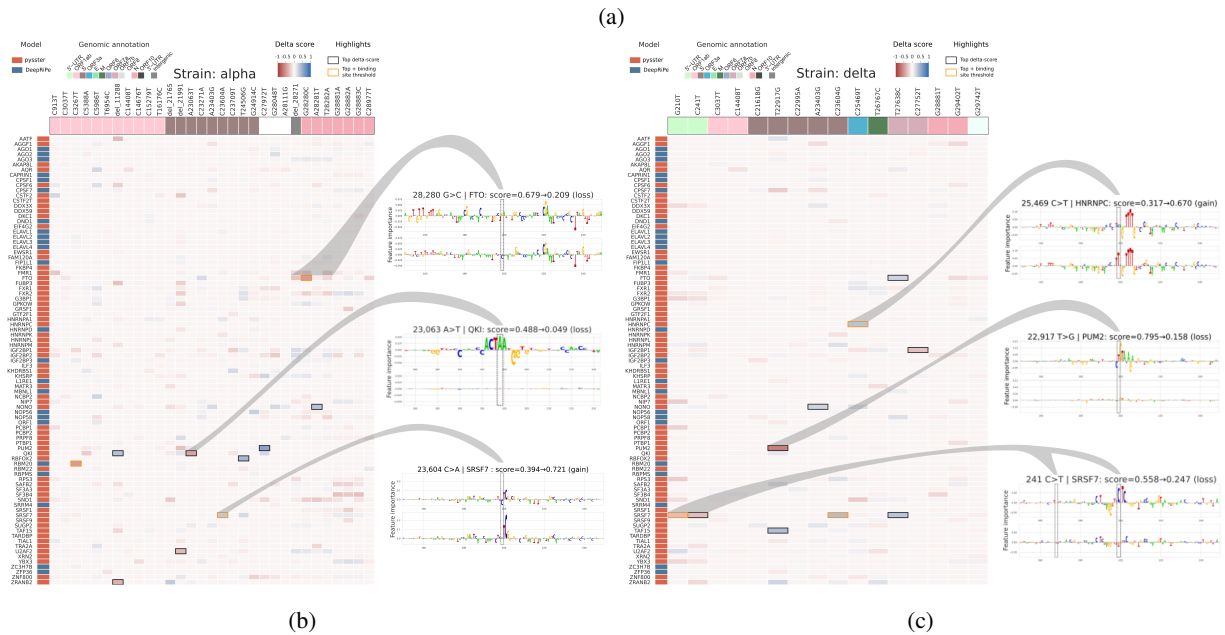
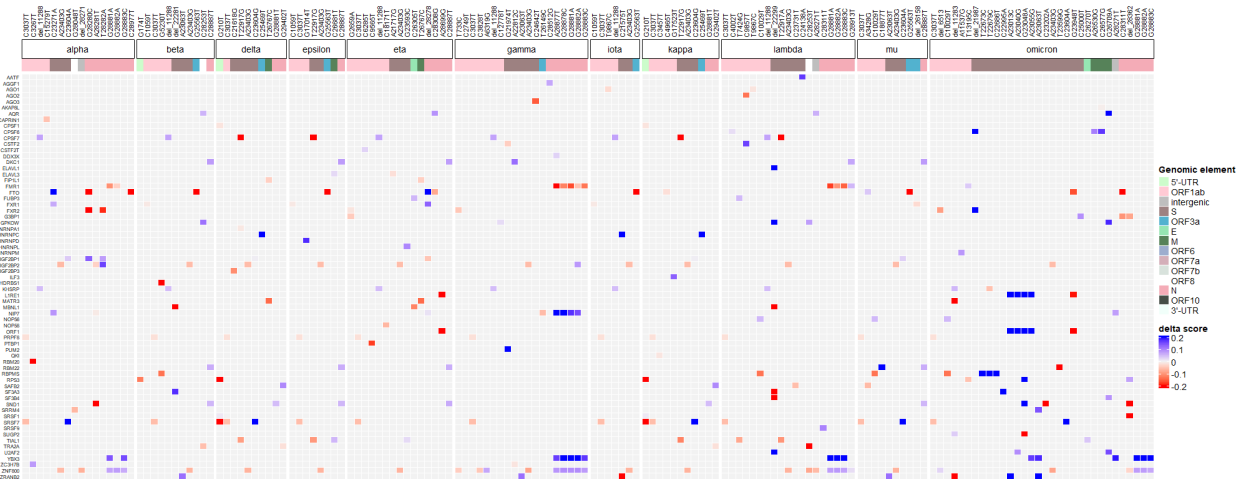
## COMPUTATIONAL MAPPING OF THE HUMAN-SARS-CoV-2 PROTEIN-RNA INTERACTOME



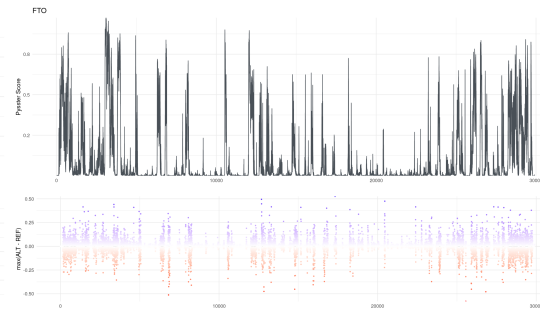
## COMPUTATIONAL MAPPING OF THE HUMAN-SARS-CoV-2 PROTEIN-RNA INTERACTOME

Figure 3: Computational map of RBP binding on SARS-CoV-2. **a** Single-nucleotide probability score for RBFOX2 (left) and TARDBP (right) RBP binding as computed by the corresponding pysster models across the whole SARS-CoV-2 genome. The higher the score, the higher the likelihood of a binding event at that position. Points highlighted in strong color correspond to significant predictions, i.e. with bound probability significantly higher than random (empirical p-value < 0.01, see Methods). Wider binding sites, encompassing more than one significant position are shown as vertical bars underneath each prediction profile, together with their corresponding binding motifs as extracted by means of attribution maps (see Methods). **b** Single-nucleotide probability score for MBNL1 (left) and QKI (right) RBP binding as computed by the corresponding DeepRiPe models. Significant positions (empirical p-value < 0.01) are highlighted in strong color, and computed binding sites together with their corresponding motifs are shown underneath. **c** Clustering of RBPs based on binding site coverage of genomic annotations of SARS-CoV-2 for both pysster and DeepRiPe RBPs (left panel). *In silico* RBP binding map, at single-nucleotide resolution, for both pysster and DeepRiPe RBPs (right panel). SARS-CoV-2 SECRETE motifs from (27) are shown below.

COMPUTATIONAL MAPPING OF THE HUMAN-SARS-CoV-2 PROTEIN-RNA INTERACTOME



(d)

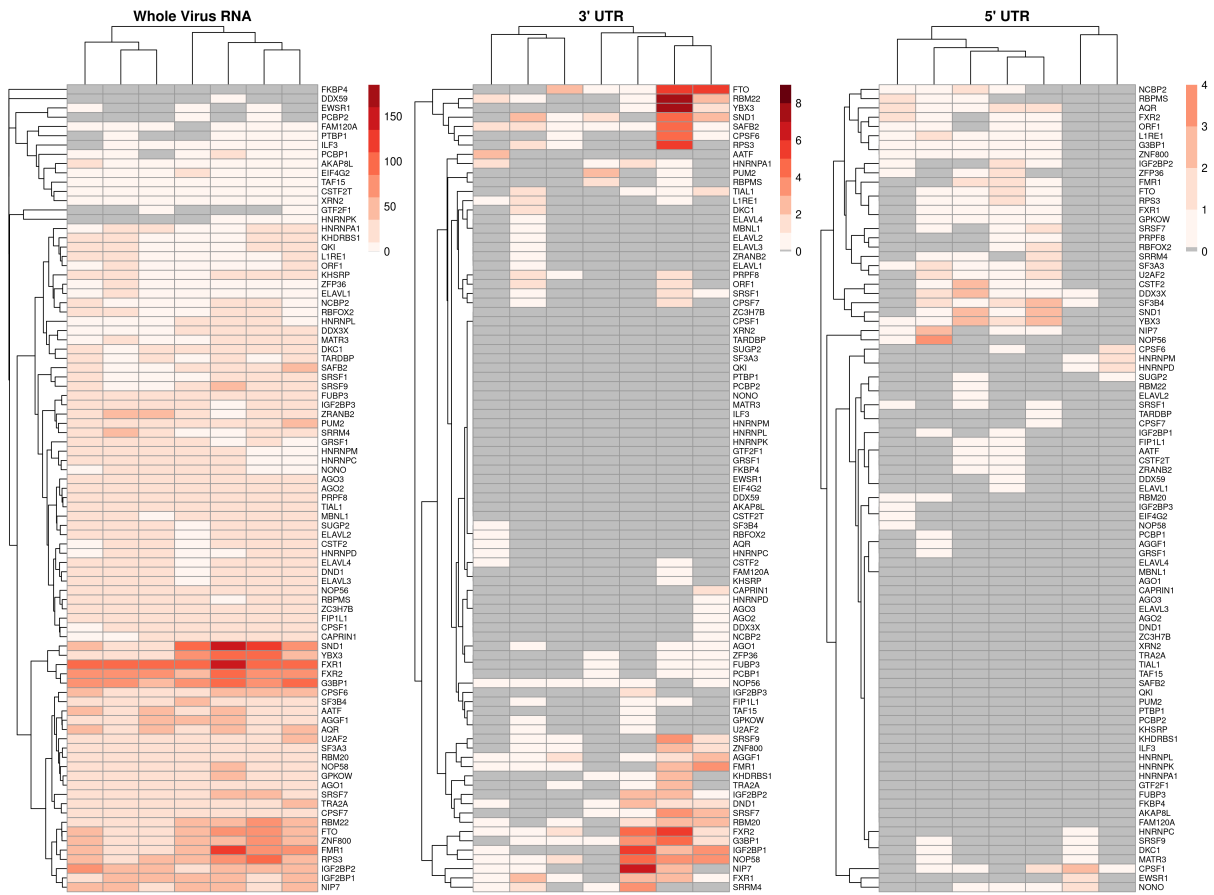


(e)

## COMPUTATIONAL MAPPING OF THE HUMAN-SARS-CoV-2 PROTEIN-RNA INTERACTOME

Figure 4: Impact of variants from SARS-CoV-2 strains on predicted binding sites. **a.** Joint heatmap of delta scores from the 290 identified variants in the different SARS-CoV-2 strains. Delta-scores represent the difference in prediction score of a prediction model between alternative and reference sequences centered on each variant. Only the 315 impacts labeled as change-of-binding are colored (see 3.11). Delta score color scale is capped so as to show low delta score impacts. RBPs and mutations without any such impact across strains are dropped from the heatmap. **b.** Complete heatmap of delta scores from 31 variants associated to the alpha viral variant. The top 10 with highest absolute delta scores are lined out, with yellow color indicating the ones labeled as change-of-binding. Some sites are further investigated through integrated gradients, comparing the sequence motifs identified by the prediction models against known motifs from mCrossBase (16). **c.** Complete heatmap of delta scores from 16 variants associated to the delta viral variant. **d,e.** Results from the *in silico* mutagenesis over the SARS-CoV-2 genome. Nucleotides across the viral genome were perturbed towards the three alternative bases, generating a reference distribution of possible delta-scores, notably highlighting positions with highest impacts. Here, **d**) and **e**) display the position-wise reference score (top) and delta score (bottom) for PUM2 and FTO, respectively.

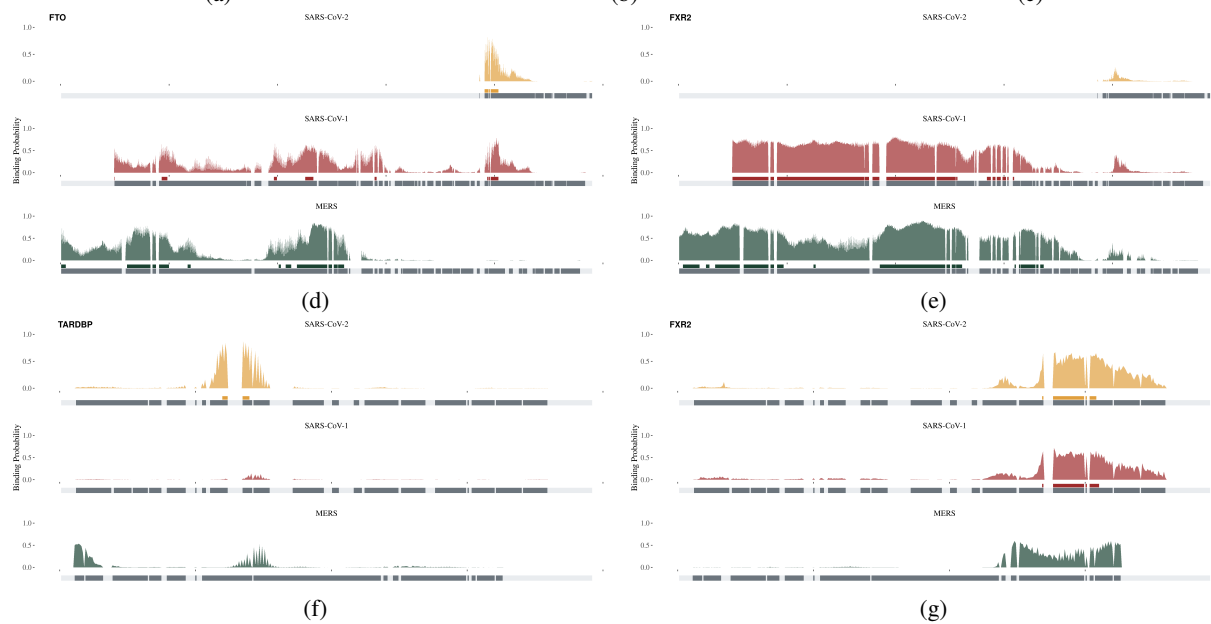
COMPUTATIONAL MAPPING OF THE HUMAN-SARS-CoV-2 PROTEIN-RNA INTERACTOME



(a)

(b)

(c)



(d)

(e)

(f)

(g)

## COMPUTATIONAL MAPPING OF THE HUMAN-SARS-CoV-2 PROTEIN-RNA INTERACTOME

Figure 5: Comparison of SARS-CoV-2 and 6 other human coronaviruses. **a,b,c.** Binding sites were predicted over the seven human coronaviruses, and their number counted over the entire genome (**a**) or over the 3' (**b**) and 5' (**c**) UTRs. Hierarchical clustering was applied to evaluate the proximity between viruses in terms of binding sites composition. **d,e,f,g.** Examples of evolutionary conserved, gained, and lost binding sites between the three high-severity viruses MERS, SARS-CoV-1, and SARS-CoV2. Panel **d** shows an example for FTO binding sites found only in SARS-Cov-2 and SARS-CoV-1 in their 3' UTRs. Panel **e** shows a binding site for FXR2 only shared between MERS and SARS-CoV-1 in their 3' UTR. Panel **f** shows a binding site for TARDBP exclusive to SARS-CoV-2 in the 5' UTR. Panel **g** shows a binding site for FXR2 only shared between SARS-CoV-2 and SARS-CoV-1 in the 5' UTR.

COMPUTATIONAL MAPPING OF THE HUMAN-SARS-CoV-2 PROTEIN-RNA INTERACTOME

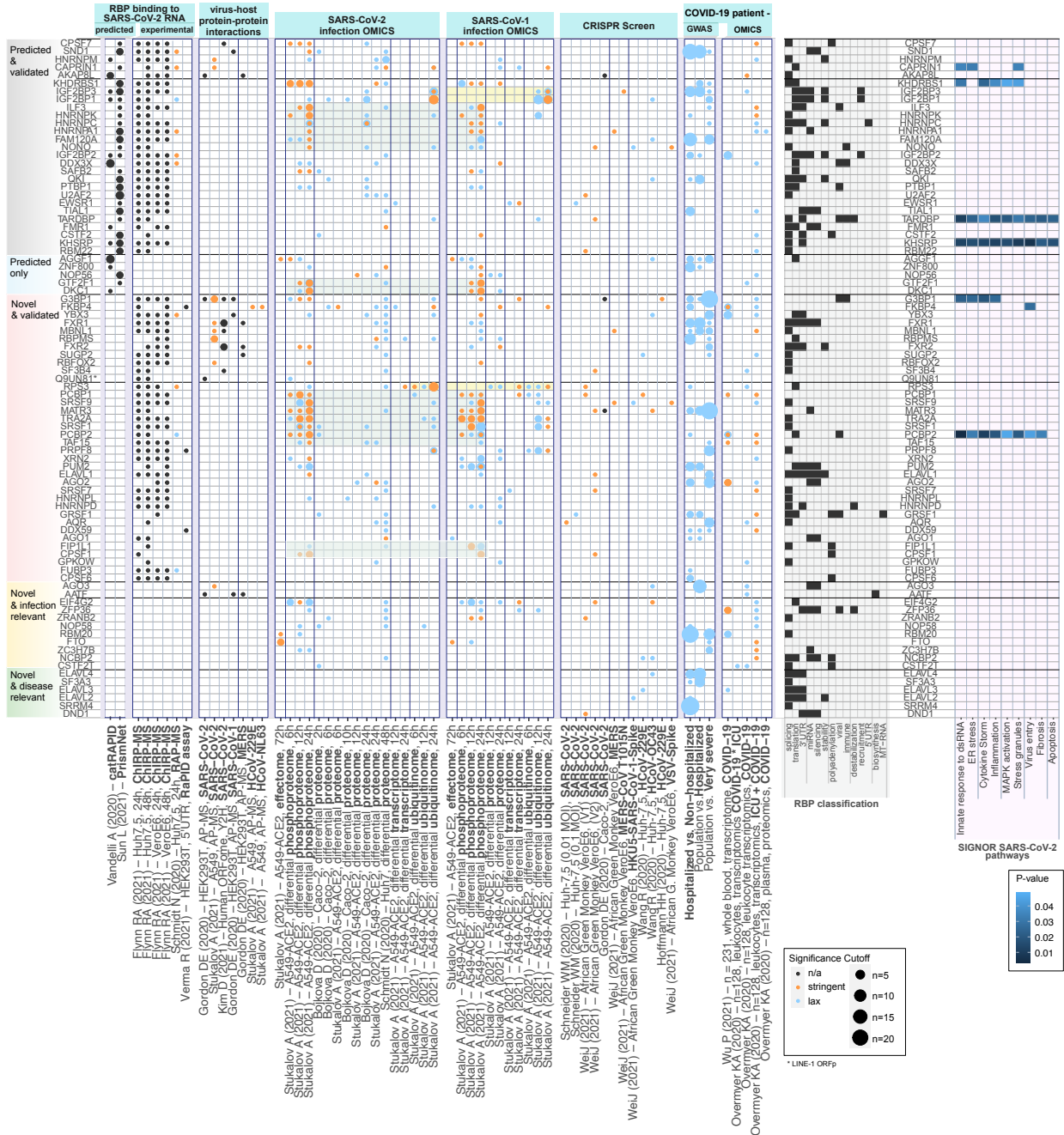


Figure 6: **RBPs in context of public *in vitro* and patient OMICS data.** RBP with model predictions (rows) annotated with experimental evidences found in 92 multiOMIC publicly available research results (columns) followed by information from RBP classification and role in known SARS-CoV-2 pathways. From left to right: RBPs were manually assigned to five categories according to their annotation pattern. RBPs predicted to bind SARS-CoV-2 RNA by the other prediction methods catRAPID, PrismNET. RBPs binding to SARS-CoV-2 RNA determined experimentally by ChIRP-MS, RAP-MS and RAPID assay. Evidences of RBPs with stringent or lax significance cutoffs found in further 55 data sets across multiple OMICS levels and experiment types were grouped by experimental context: Experimental viral-host protein interactions measured by AP-MS across various coronaviruses, SARS-CoV-2 and SARS-CoV-2 infection OMIC (timecourses), selected CRISPR studies, most recent GWAS data (release 6) by Host Genetics Initiative and blood-based patient OMICS data. Light green and yellow boxed highlight few patterns shared between SARS-CoV-2 and -1 infections. Classification of RBP according to their roles related to biological processes. Far right: Annotation of RBPs to pathways related to SARS-CoV-2 infections obtained from SIGNOR database.



COMPUTATIONAL MAPPING OF THE HUMAN-SARS-CoV-2 PROTEIN-RNA INTERACTOME

1077 **8 Supplementary Tables**

Supplementary Table 1: Comparison of high quality pysster and DeepRiPe models

RBP	cor of pred score	cor of p-value	# common binding sites
TARDBP	0.640832	0.40309	6
CSTF2	0.459011	0.21621	6
IGF2BP1	0.387823	0.39983	9
PUM2	0.383309	0.35263	10
CSTF2T	0.331395	0.22239	3
QKI	0.279760	0.14371	5
IGF2BP2	0.171838	0.21092	7
IGF2BP3	0.073798	0.05951	5
CPSF6	0.153344	0.26078	2
FXR1	0.012354	0.14136	8
FXR2	0.080191	0.19433	5
EWSR1	0.009787	0.06610	0

Supplementary Table 2: Overlap of pysster and DeepRiPe binding sites with SECRETE motif

RBP	# overlaps	# binding sites	Ratio	Model	Binding sites
FUBP3	7	20	0.350	pysster	[11040,11049], [11068,11118], [14155,14165], [14383,14391], [21920,21928], [26299,26317], [26336,26344]
PTBP1	1	3	0.333	pysster	[9500,9584]
KHSRP	5	16	0.312	pysster	[8596,8635], [9496,9530], [11287,11326], [14142,14172], [26293,26351]
SUGP2	7	24	0.292	pysster	[9622,9652], [11091,11116], [11191,11231], [11278,11368], [11626,11663], [21580,21596], [27831,27848]
ELAVL4	4	14	0.286	DeepRiPe	[8622,8624], [11028,11065], [27677,27685], [27802,27824]
ZFP36	2	7	0.286	DeepRiPe	[8595,8613], [21928,21932]
ELAVL2	5	18	0.278	DeepRiPe	[8612,8624], [11029,11067], [21563,21565], [21911,21942], [27795,27827]
ELAVL3	4	15	0.267	DeepRiPe	[9523,9527], [11041,11065], [21920,21933], [27800,27826]
MBNL1	5	19	0.263	DeepRiPe	[11645,11657], [15492,15524], [26288,26341], [27164,27199], [27792,27853]
MATR3	4	16	0.250	pysster	[9511,9539], [11182,11313], [11614,11658], [26303,26324]
AGO2	4	18	0.222	DeepRiPe	[8589,8631], [15528,15582], [24091,24134], [28722,28730]
NCBP2	2	9	0.222	pysster	[12026,12027], [14770,14772]
ZNF800	8	39	0.205	pysster	[1659,1701], [3826,4059], [12025,12234], [14769,14774], [14800,14882], [15529,15533], [28692,28764], [28911,28957]
CSTF2	2	10	0.200	pysster	[8591,8633], [13883,13912]
QKI	3	15	0.200	pysster	[9521,9533], [11326,11347], [14167,14178]

COMPUTATIONAL MAPPING OF THE HUMAN-SARS-CoV-2 PROTEIN-RNA INTERACTOME

DDX3X	3	17	0.176	pysster	[12026,12030], [14769,14772], [28861,28949]
TARDBP	2	12	0.167	pysster	[11117,11123], [11218,11388]
G3BP1	12	83	0.145	pysster	[818,841], [1651,1731], [3787,4196], [8168,8346], [12026,12376], [14396,14397], [14769,14824], [14836,14908], [15519,15531], [16524,16810], [28386,28753], [28913,28974]
GRSF1	1	7	0.143	pysster	[28891,28903]
HNRNPC	2	14	0.143	pysster	[9787,9789], [11034,11044]
CPSF6	6	45	0.133	pysster	[1707,1715], [3808,4054], [4090,4098], [11182,11214], [21938,21969], [26333,26352]
FIP1L1	2	15	0.133	DeepRiPe	[13900,13935], [21935,21971]
SF3B4	4	30	0.133	pysster	[11959,12000], [16553,16561], [21527,21529], [24083,24101]
U2AF2	4	31	0.129	pysster	[9773,9777], [12004,12023], [14379,14392], [27785,27839]
DKC1	2	16	0.125	pysster	[779,889], [14769,14801]
NONO	1	8	0.125	pysster	[11204,11222]
NIP7	5	43	0.116	pysster	[806,834], [13880,13945], [14763,14797], [16536,16546], [25236,25254]
CPSF1	3	28	0.107	DeepRiPe	[827,841], [23278,23312], [28914,28946]
GPLOW	3	28	0.107	pysster	[11982,12026], [21575,21579], [26302,26310]
SRSF9	3	28	0.107	pysster	[821,834], [12026,12028], [28850,28915]
FXR1	11	106	0.104	pysster	[639,928], [1631,1703], [1715,1723], [3963,4107], [8619,8627], [13907,13913], [14771,14876], [15506,15549], [16543,16555], [23231,23266], [27401,27417]
AKAP8L	1	10	0.100	pysster	[14786,14788]
AATF	2	22	0.091	pysster	[5698,5702], [15525,15568]
ZRANB2	3	34	0.088	pysster	[11655,11661], [21574,21586], [26284,26330]
AGGF1	3	35	0.086	pysster	[4031,4057], [12024,12088], [14766,14776]
FMR1	5	59	0.085	pysster	[750,839], [858,910], [14879,14891], [23268,23276], [28859,28908]
HNRNPD	1	12	0.083	DeepRiPe	[9492,9522]
HNRNPM	1	12	0.083	pysster	[11345,11384]
NOP56	1	12	0.083	DeepRiPe	[814,821]
SRSF7	3	38	0.079	pysster	[820,838], [14771,14811], [23253,23280]
CPSF7	2	27	0.074	DeepRiPe	[14849,14875], [21924,21929]
FXR2	5	70	0.071	pysster	[3776,4047], [4059,4063], [12024,12268], [13905,13957], [14770,14775]
ORF1	1	14	0.071	DeepRiPe	[28693,28703]
FTO	4	58	0.069	pysster	[12021,12131], [14795,14809], [23258,23266], [28679,28778]
RBM22	3	45	0.067	pysster	[4029,4057], [26286,26336], [28834,28935]

COMPUTATIONAL MAPPING OF THE HUMAN-SARS-CoV-2 PROTEIN-RNA INTERACTOME

YBX3	4	60	0.067	pysster	[705,870], [14767,14855], [14891,14919], [23295,23327]
SF3A3	2	34	0.059	pysster	[11965,12009], [16529,16601]
SRRM4	1	17	0.059	DeepRiPe	[26278,26328]
PRPF8	1	19	0.053	pysster	[27150,27193]
RPS3	3	57	0.053	pysster	[730,941], [14769,14776], [28568,28740]
AGO3	1	20	0.050	DeepRiPe	[28710,28752]
SND1	4	82	0.049	pysster	[750,852], [14771,14772], [23266,23287], [28697,28720]
AGO1	1	22	0.045	DeepRiPe	[28712,28771]
SAFB2	2	44	0.045	pysster	[1688,1710], [4042,4062]
SRSF1	1	22	0.045	pysster	[12024,12028]
TRA2A	2	47	0.043	pysster	[12025,12055], [14766,14774]
TIAL1	1	27	0.037	pysster	[26271,26318]
PUM2	1	29	0.034	pysster	[27141,27165]
AQR	1	30	0.033	pysster	[11957,12027]
RBM20	1	30	0.033	DeepRiPe	[28728,28736]
IGF2BP1	1	50	0.020	pysster	[28657,28722]
CAPRIN1	0	19	0.000	DeepRiPe	
CSTF2T	0	3	0.000	pysster	
DDX59	0	0	0.000	pysster	
DND1	0	14	0.000	DeepRiPe	
EIF4G2	0	5	0.000	pysster	
ELAVL1	0	7	0.000	DeepRiPe	
EWSR1	0	0	0.000	pysster	
FAM120A	0	2	0.000	pysster	
FKBP4	0	0	0.000	pysster	
GTF2F1	0	1	0.000	pysster	
HNRNPA1	0	16	0.000	pysster	
HNRNPK	0	1	0.000	pysster	
HNRNPL	0	9	0.000	pysster	
IGF2BP2	0	50	0.000	pysster	
IGF2BP3	0	23	0.000	DeepRiPe	
ILF3	0	9	0.000	pysster	
KHDRBS1	0	10	0.000	pysster	
L1RE1	0	13	0.000	DeepRiPe	
NOP58	0	26	0.000	DeepRiPe	
PCBP1	0	8	0.000	pysster	
PCBP2	0	0	0.000	pysster	
RBFOX2	0	8	0.000	pysster	
BPMS	0	19	0.000	DeepRiPe	

COMPUTATIONAL MAPPING OF THE HUMAN-SARS-CoV-2 PROTEIN-RNA INTERACTOME

TAF15	0	5	0.000	pysster
XRN2	0	2	0.000	pysster
ZC3H7B	0	20	0.000	DeepRiPe

Supplementary Table 3: Overlap of pysster and DeepRiPe models with proteins from external sources

RBP	pysster			DeepRiPe		Overlaps with proteins from external sources											SIGNOR*	
	auROC	auPRC	medPIP	auROC	AP	(40)	(24)	(92)	(70)	(69)	(18)	(87)	(4)	(46)	(78)	(80)		
AATF	0.92	0.66	0.1				X											
AGGF1	0.91	0.71	0.17								X			X <sup>15</sup>				
AGO1				0.79	0.32				X <sup>4</sup>									
AGO2				0.85	0.5													
AGO3				0.87	0.49													
AKAP8L	0.89	0.6	0.21			X					X							
AQR	0.93	0.7	0.22					X										
CAPRIN1				0.76	0.22				X <sup>234</sup>					X <sup>1416</sup>		X <sup>18</sup>	Innate response to dsRNA, ER stress, Stress granules	
CPSF1				0.77	0.23		X							X <sup>1516</sup>				
CPSF6	0.89	0.61	0.18	0.79	0.26													
CPSF7				0.79	0.54							X <sup>6</sup>		X <sup>1516</sup>		X <sup>18</sup>		
CSTF2	0.93	0.81	0.14	0.82	0.3											X <sup>1718</sup>		
CSTF2T	0.92	0.6	0.19	0.84	0.66													
DDX3X	0.96	0.78	0.32						X <sup>23</sup>		X		X <sup>10</sup>	X <sup>15</sup>				
DDX59	0.89	0.67	0.16						X <sup>4</sup>									
DKC1	0.96	0.89	0.21								X			X <sup>1516</sup>				
DND1				0.82	0.46													
EIF4G2	0.95	0.78	0.31					X	X <sup>4</sup>					X <sup>1516</sup>				
ELAVL1				0.9	0.73			X		X		X <sup>67</sup>	X <sup>8</sup>	X <sup>1516</sup>				
ELAVL2				0.93	0.61													
ELAVL3				0.94	0.72													
ELAVL4				0.93	0.58													
EWSR1	0.93	0.62	0.22	0.85	0.2			X <sup>1</sup>					X <sup>9</sup>	X <sup>1216</sup>		X <sup>18</sup>		
FAM120A	0.92	0.62	0.24							X			X <sup>8</sup>	X <sup>1516</sup>		X <sup>1718</sup>		
FIP1L1				0.8	0.3				X <sup>4</sup>					X <sup>1516</sup>				
FKBP4	0.93	0.65	0.18									X <sup>7</sup>		X <sup>1416</sup>			Virus entry	
FMR1	0.94	0.67	0.18						X <sup>4</sup>		X		X <sup>10</sup>					
FTO	0.92	0.63	0.27															
FUBP3	0.95	0.8	0.14						X <sup>23</sup>					X <sup>8</sup>				
FXR1	0.92	0.6	0.26	0.86	0.26	X								X <sup>8</sup>				
FXR2	0.94	0.67	0.23	0.8	0.18	X								X <sup>10</sup>				
G3BP1	0.93	0.64	0.31			X	X		X <sup>234</sup>					X <sup>8</sup>	X <sup>111516</sup>			Innate response to dsRNA, Inflammation, ER stress, Cytokine Storm
GPKOW	0.92	0.71	0.16					X										
GRSF1	0.93	0.71	0.18					X	X <sup>4</sup>									
GTF2F1	0.94	0.71	0.29						X <sup>4</sup>					X <sup>15</sup>		X <sup>17</sup>		
HNRNPA1	0.94	0.74	0.11						X <sup>23</sup>	X				X <sup>15</sup>		X <sup>1718</sup>		
HNRNPC	0.97	0.83	0.15							X		X <sup>67</sup>		X <sup>1516</sup>		X <sup>18</sup>		
HNRNPD				0.94	0.47							X <sup>7</sup>	X <sup>10</sup>	X <sup>1516</sup>				
HNRNPK	0.98	0.87	0.3							X		X <sup>67</sup>		X <sup>1516</sup>		X <sup>17</sup>		
HNRNPL	0.97	0.86	0.31						X <sup>23</sup>	X		X <sup>6</sup>	X <sup>10</sup>					
HNRNPM	0.95	0.74	0.22				X			X	X	X <sup>7</sup>	X <sup>9</sup>					
IGF2BP1	0.91	0.66	0.12	0.83	0.19				X <sup>23</sup>	X	X	X <sup>6</sup>		X <sup>1416</sup>		X <sup>17</sup>		
IGF2BP2	0.91	0.65	0.13	0.84	0.29				X <sup>2</sup>		X			X <sup>8</sup>		X <sup>17</sup>		
IGF2BP3	0.88	0.56	0.08	0.84	0.42					X	X			X <sup>8</sup>	X <sup>14</sup>	X <sup>1718</sup>		
ILF3	0.93	0.74	0.15						X <sup>4</sup>				X <sup>7</sup>	X <sup>9</sup>	X <sup>1516</sup>	X <sup>17</sup>		

COMPUTATIONAL MAPPING OF THE HUMAN-SARS-CoV-2 PROTEIN-RNA INTERACTOME

KHDRBS1	0.97	0.86	0.18							X			X <sup>9</sup>	X <sup>1516</sup>		X <sup>1718</sup>	Innate response to dsRNA, Inflammation, MAPK activation, Stress granules, Cytokine Storm
KHSRP	0.9	0.65	0.15							X	X			X <sup>1516</sup>		X <sup>1718</sup>	Apoptosis, Fibrosis, Innate response to dsRNA, Virus entry, Inflammation, ER stress, MAPK activation, Stress granules, Cytokine Storm
LIRE1				0.96	0.59		X			X							
MATR3	0.94	0.7	0.23					X	X <sup>4</sup>	X			X <sup>8</sup>	X <sup>1516</sup>			
MBNL1				0.98	0.94									X <sup>16</sup>			
NCBP2	0.93	0.71	0.24														
NIP7	0.92	0.69	0.15										X <sup>7</sup>				
NONO	0.92	0.6	0.15	0.93	0.38		X						X <sup>7</sup>	X <sup>89</sup>	X <sup>1516</sup>	X <sup>17</sup>	
NOP56				0.92	0.69									X <sup>1516</sup>		X <sup>1718</sup>	
NOP58				0.93	0.68				X <sup>4</sup>								
ORF1p				0.97	0.67												
PCBP1	0.93	0.67	0.16										X <sup>10</sup>	X <sup>1516</sup>			
PCBP2	0.96	0.79	0.3					X	X <sup>23</sup>					X <sup>15</sup>			Fibrosis, Innate response to dsRNA, Virus entry, Inflammation, ER stress, MAPK activation, Stress granules, Cytokine Storm
PRPF8	0.95	0.74	0.33											X <sup>14</sup>			
PTBP1	0.94	0.8	0.37							X			X <sup>67</sup>	X <sup>8</sup>	X <sup>1516</sup>	X <sup>1718</sup>	
PUM2	0.95	0.8	0.16	0.95	0.72								X <sup>10</sup>	X <sup>1516</sup>			
QKI	0.97	0.87	0.31	0.97	0.64											X <sup>1718</sup>	
RBFOX2	0.96	0.8	0.24											X <sup>1516</sup>			
RBM20				0.91	0.59												
RBM22	0.91	0.72	0.2													X <sup>1718</sup>	
RBPMS				0.97	0.78										X <sup>13</sup>		
RPS3	0.94	0.63	0.28						X <sup>234</sup>				X <sup>10</sup>	X <sup>12141516</sup>			
SAFB2	0.93	0.7	0.11										X <sup>9</sup>	X <sup>15</sup>		X <sup>18</sup>	
SF3A3	0.96	0.84	0.23														
SF3B4	0.98	0.88	0.26				X	X									
SND1	0.95	0.75	0.21						X <sup>234</sup>				X <sup>5</sup>	X <sup>8</sup>	X <sup>15</sup>	X <sup>1718</sup>	
SRRM4				0.8	0.31												
SRSF1	0.94	0.7	0.28							X			X <sup>67</sup>	X <sup>1516</sup>			
SRSF7	0.92	0.69	0.17				X		X <sup>4</sup>	X				X <sup>16</sup>			
SRSF9	0.92	0.65	0.18											X <sup>141516</sup>			
SUGP2	0.9	0.63	0.15						X <sup>4</sup>								
TAF15	0.93	0.7	0.17	0.88	0.28									X <sup>15</sup>			
TARDBP	0.98	0.92	0.28	0.95	0.73		X			X						X <sup>18</sup>	Apoptosis, Fibrosis, Innate response to dsRNA, Virus entry, Inflammation, ER stress, MAPK activation, Stress granules, Cytokine Storm
TIAL1	0.95	0.8	0.13						X <sup>4</sup>				X <sup>10</sup>			X <sup>1718</sup>	
TRA2A	0.96	0.8	0.29											X <sup>141516</sup>			
U2AF2	0.95	0.77	0.15										X <sup>67</sup>			X <sup>1718</sup>	
XRN2	0.93	0.64	0.18											X <sup>15</sup>			
YBX3	0.92	0.71	0.1						X <sup>2</sup>				X <sup>8</sup>				
ZC3H7B				0.87	0.37												
ZFP36				0.93	0.46				X <sup>4</sup>					X <sup>1516</sup>			
ZNF800	0.93	0.62	0.25						X <sup>4</sup>		X			X <sup>15</sup>			
ZRANB2	0.9	0.64	0.1						X <sup>4</sup>								

<sup>1</sup> also included in the PPI network

<sup>2</sup> SARS-CoV-2 RNA interacting proteins

<sup>3</sup> proteins included in the PPI network (network based on STRING v.11 interactions between human proteins in the expanded SARS-CoV-2 RNA interactome)

<sup>4</sup> differentially expressed proteins (SARS-CoV-2 infected and uninfected Huh7 cells)

<sup>5</sup> proteins that were reduced during SARS-CoV-2 infection

<sup>6</sup> proteins that increased during SARS-CoV-2 infection

<sup>7</sup> additional potential inhibitors of SARS-CoV-2 replication

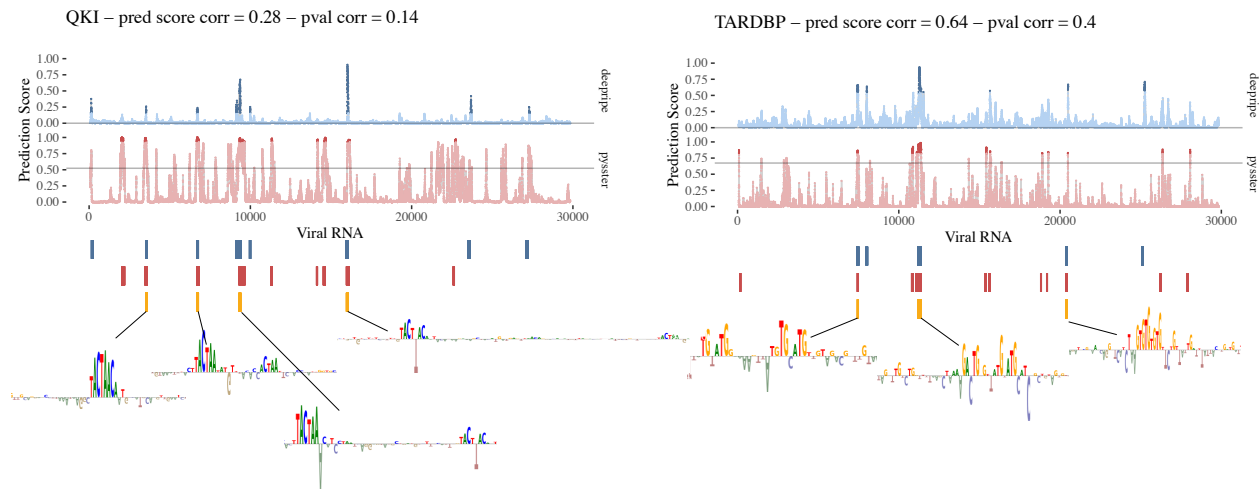
<sup>8</sup> statistically significant interactors enriched in both probe I and probe II experiment

## COMPUTATIONAL MAPPING OF THE HUMAN-SARS-CoV-2 PROTEIN-RNA INTERACTOME

- <sup>9</sup> statistically significant interactors enriched in only probe I experiment
- <sup>10</sup> statistically significant interactors enriched in only probe II experiment
- <sup>11</sup> proteins included in virus-host PPI network of SARS-CoV-2 in A549 cells
- <sup>12</sup> transcripts that significantly change upon SARS-CoV-2 infection
- <sup>13</sup> proteins that significantly change upon SARS-CoV-2 infection
- <sup>14</sup> ubiquitination site significantly changes upon SARS-CoV-2 infection
- <sup>15</sup> phosphorylation site significantly changes upon SARS-CoV-2 infection
- <sup>16</sup> included in results of enrichment analysis
- <sup>17</sup> RBPs predicted to bind the 5'UTR of SARS-CoV-2
- <sup>18</sup> RBPs predicted to bind the 3'UTR of SARS-CoV-2
- \* empirical p-value < 0.05

## COMPUTATIONAL MAPPING OF THE HUMAN-SARS-CoV-2 PROTEIN-RNA INTERACTOME

### 1078 9 Supplementary Figures



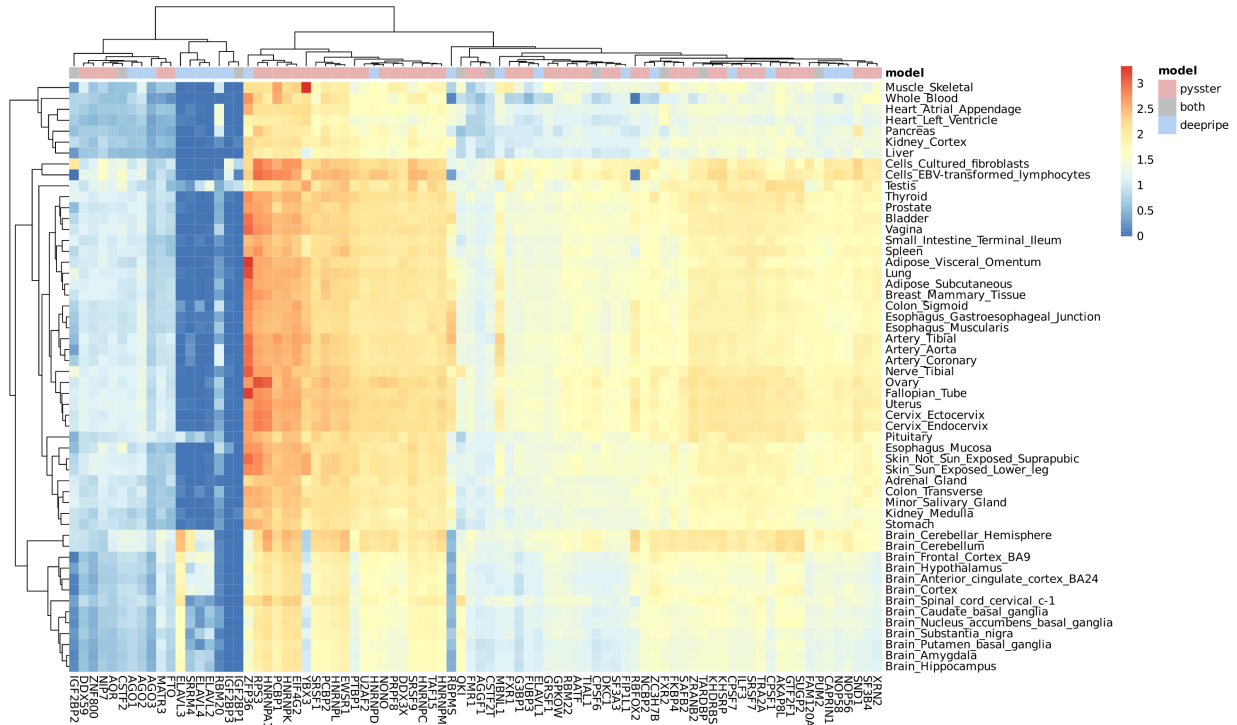
Supplementary Figure 1: RBP binding pattern on the SARS-CoV-2 genome between the two methods, pysster and DeepRiPe. Comparison of single-nucleotide probability scores of binding for two RBPs, QKI (left panel) and TARDBP (right panel). Significant binding sites, commonly predicted by both methods are shown underneath the probability plots together with their corresponding learnt motifs from the attribution maps. Prediction score correlation and p-value correlation given in the header.







## COMPUTATIONAL MAPPING OF THE HUMAN-SARS-COV-2 PROTEIN-RNA INTERACTOME



Supplementary Figure 4: Expression of RBPs in tissues across the body: Median expression values in log<sub>10</sub> transcript per million (TPM) of RBPs across 54 sub-tissue types from the Genotype-Tissue Expression (GTEx) project (7). RBPs from different methods color coded above the heatmap: pysster-exclusive in red, DeepRiPe-exclusive in blue, and shared between models in grey.